The Astrophysical Journal, 923:185 (17pp), 2021 December 20 https://doi.org/10.3847/1538-4357/ac2eb3

Low-frequency Waves due to Newborn Interstellar Pickup He^+ Observed by the Ulysses Spacecraft

Anastasia V. Marchuk[1], Charles W. Smith[1], Abigale S. Watson[1,4], Matthew R. Argall[1], Colin J. Joyce[1], Philip A. Isenberg[1], Bernard J. Vasquez[1], Nathan A. Schwadron[1], Maciej Bzowski[2], Marzena A. Kubiak[2], and Neil Murphy[3]

[1] Physics Department and Space Science Center, Morse Hall, University of New Hampshire, Durham, NH, USA; Anastasia.V.Marchuk@gmail.com, Charles.Smith@unh.edu, abbey@tage.com, Matthew.Argall@unh.edu, Colin.Joyce@unh.edu, Phil.Isenberg@unh.edu, Bernie.Vasquez@unh.edu, Nathan.Schwadron@unh.edu

[2] Space Research Centre, Polish Academy of Sciences, (CBK PAN), Warsaw, Bartycka 18A, Poland; Bzowski@cbk.waw.pl, MKubiak@cbk.waw.pl

[3] Jet Propulsion Laboratory, Mail Stop 180-600, 4800 Oak Grove Drive, Pasadena, CA 91109, USA; Neil.Murphy@jpl.nasa.gov

Received 2021 August 24; revised 2021 October 2; accepted 2021 October 5; published 2021 December 21

Abstract

We have surveyed magnetic field data from the Ulysses spacecraft and found examples of magnetic waves with the expected characteristics that point to excitation by newborn pickup He^+. With interstellar neutrals as the likely source for the pickup ions, we have modeled the ion production rates and used them to produce wave excitation rates that we compare to the background turbulence rates. The source ions are thought to be always present, but the waves are seen when growth rates are comparable to or exceed the turbulence rates. With the exception of the fast latitude scans, and unlike the waves excited by newborn interstellar pickup H^+, the waves are seen throughout the Ulysses orbit.

Unified Astronomy Thesaurus concepts: Heliosphere (711); Solar wind (1534); Pickup ions (1239); Interplanetary turbulence (830); Alfven waves (23)

1. Introduction

The expanding solar wind, which carries the Sun's magnetic field outward, forms a magnetohydrodynamic fluid that gives structure to the heliosphere. The dynamics of the magnetized plasma in the variable flow lead to the formation of shocks, interaction regions, rarefaction regions, and the interaction of the solar wind with planetary magnetic fields. The large-scale structure controls the propagation of energetic charged particles throughout the heliosphere. However, interstellar neutral atoms pass through this expanding magnetized plasma at a velocity that reflects the motion of the Sun through local interstellar space at $\sim$25 km s^{-1} (Bzowski et al. 2012, 2015; McComas et al. 2012, 2015, 2017; Möbius et al. 2012; Schwadron et al. 2015). It is not until the neutral atoms are ionized that they begin to interact with the heliospheric plasma.

The two dominant ionization processes are collision with solar wind protons for H^+ production and collision with extreme ultraviolet (EUV) solar photons for He^+ production (Sokół et al. 2020). Neutral H is the dominant interstellar atom, but ionization of H is more efficient such that neutral H is depleted inside $\sim$3.5 au, while the less effective neutralization of He leads to He^+ production closer to the Sun.

Once ionized, the newborn, singly charged, pickup ion (PUI) streams along the magnetic field at nearly the solar wind speed in the plasma frame when the magnetic field is radial. In contrast, when the field is transverse to the radial direction, the newborn pickup ion has a velocity that is largely perpendicular to the magnetic field with reduced sunward streaming along the field. This is because the neutral atom is nearly stationary in the solar frame, and the pickup process is largely unrelated to the inflow direction of the neutral atoms. Apart from any systematic variation associated with the mean field direction and wind speed, the pickup process is independent of the solar cycle, heliocentric distance, and latitude. The neutral atom density will vary, but the local dynamics, including wave generation, will be the same. The cyclotron resonant instability leads to the excitation of low-frequency magnetic waves that are seen to be sunward-propagating and left-hand polarized at the cyclotron frequency of the source ion in the spacecraft frame. Only a small number of interstellar pickup H^+ is seen inside $\sim$3.5 au because the ionization is efficient and depletes the neutral H atoms. Both interstellar pickup He^+ and the waves they excite are seen as far in as 1 au (Argall et al. 2015; Fisher et al. 2016; Hollick et al. 2018a).

We report observations by the Ulysses spacecraft of magnetic waves that are excited by newborn interstellar He^+. The observations extend throughout most of the lifetime of the Ulysses mission and are only absent during the fast latitude scans. They are seen over the full range of heliocentric distances and latitudes. Ulysses observations of wave excitation by newborn interstellar H^+ have already been reported (Murphy et al. 1995; Cannon et al. 2013, 2014a, 2014b, 2017). Likewise, excitation of waves by newborn interstellar He^+ has been reported using the Advanced Composition Explorer (ACE; Argall et al. 2015; Fisher et al. 2016), while excitation by both H^+ and He^+ pickup ions has been observed in the Voyager magnetic field data (Joyce et al. 2010, 2012; Aggarwal et al. 2016; Argall et al. 2017, 2018; Hollick et al. 2018a, 2018b, 2018c). Some of these observations are reviewed in Smith et al. (2017). What makes these observations different from previous reports is the relative abundance of the waves that are more numerous than what was seen in previous reports. As before, we observe the waves when

[4] Department of Mechanical Engineering, Wentworth Institute of Technology, Boston, Massachusetts, USA.

the background turbulence is weaker than the wave growth, thereby giving the waves the needed time to grow to observable levels.

2. Data Analysis

We analyze one-second magnetic field observations from the Flux Gate Magnetometer (FGM) instrument on the Ulysses spacecraft from shortly after launch on 1990 October 6 until the death of the spacecraft on 2009 June 30. Our first and last data intervals occur on DOY 299 of 1990 and DOY 70 of 2009, respectively. In almost every instance, there are thermal ion measurements from the Solar Wind Observations over the Poles of the Sun (SWOOPS) instrument that provide the solar wind speed and density used here. There are instances when the magnetic field data cadence slows to 4 s, but this remains adequate for the work described here.

We identified candidate data intervals both for wave events and for controls that we use to represent the unperturbed solar wind turbulence. Data intervals with large isolated discontinuities, such as shocks, yield spectra that are dominated by the large-scale structure of the interval rather than quasi-uniform fluctuations. After rejecting these, we were left with 1479 data intervals. Some intervals contain waves due to He^+, some contain waves due to H^+, and some do not contain waves other than those that make up the ambient turbulent dynamics. In this study, we extract from that ensemble two subsets. The first subset, waves due to He^+, contains 452 data intervals. The second contains 962 data intervals that are used as controls. The controls may have evidence of waves due to H^+ but are not thought to contain waves due to He^+. This is a point we will discuss below, where some interesting questions can be raised.

2.1. Data Overview

Figure 1 shows the trajectory of the Ulysses spacecraft. The spacecraft was first sent to Jupiter, where it transited the poles and was directed sunward into southern heliographic latitudes. From that point, Ulysses performed three fast latitude scans around the Sun reaching ~80° of southern and northern latitudes. In each orbit, the spacecraft returned to apoapsis at ~5 au, where Jupiter had been before returning sunward to perform another fast latitude scan.

The bottom two panels in Figure 1 show the time and duration of the data intervals used here. As a convention in this paper, the data intervals showing evidence of waves excited by He^+ are represented by red triangles, while the control intervals are represented by black squares. Three types of wave events are observed. Generally, the wave events that we can clearly attribute to pickup He^+ are represented by red triangles regardless of the quality of that determination. Note that the fast latitude scans tend to be without wave observations. This is especially true for the first solar minimum scan of 1994–95 and again after 2007.

A subset of the wave events shows strong evidence of wave activity, and we reproduce the times and durations of this list in the bottom panel where they are represented by green circles. The strong events exist within the same parts of the orbit where the weaker wave events are seen. The weak events are not singled out in this figure.

An additional event list is represented by blue plusses in Figure 1, which we keep separate from those represented by red triangles. These events show evidence of wave excitation in the

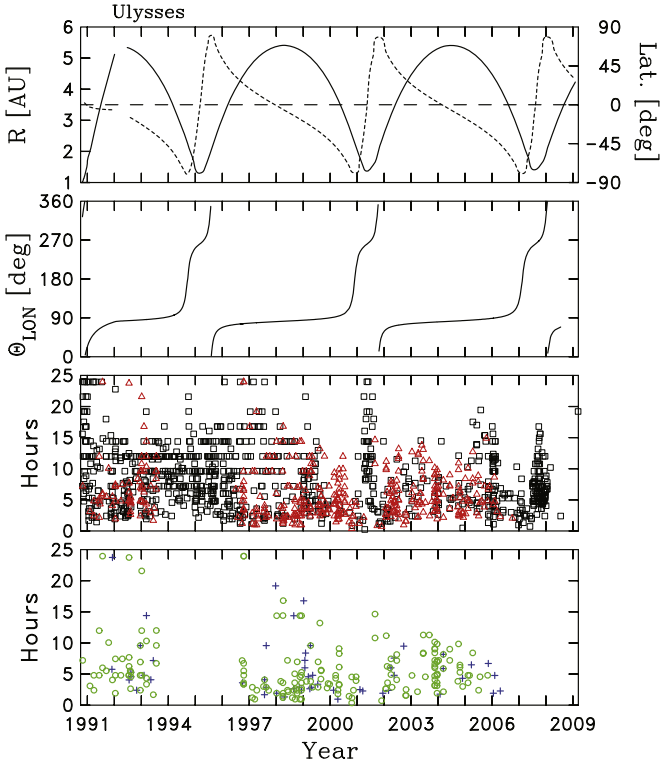

Figure 1. Trajectory of the Ulysses spacecraft. (top) Heliocentric distance R (solid curve) and heliolatitude (dashed curve) of the spacecraft as a function of time. (second panel) Heliolongitude that mostly reflects the Sun's rotation as the spacecraft orbits on a fixed plane. (third and bottom panels) Time and duration of the data intervals studied here. Red triangles represent times when wave signatures are seen at frequencies normally associated with newborn interstellar pickup He^+. Black squares represent control intervals when wave signatures are not seen in the frequency range $f_{He,c} \leqslant f_{sc} \leqslant f_{p,c}$. Control intervals may contain waves due to pickup H^+. Green circles represent the subset of wave intervals when the ellipticity $|E_{lip}| \geqslant 0.35$ averaged over the frequency range $f_{He,c} \leqslant f_{sc} \leqslant 2f_{He,c}$. Ellipticity is defined in the text. Blue plusses represent intervals when wave signatures are not present in the frequency range $f_{He,c} \leqslant f_{sc} \leqslant 2f_{He,c}$, but are present in the range $2f_{He,c} \leqslant f_{sc} \leqslant 4f_{He,c}$, suggesting acceleration of the pickup H^+ population.

frequency range normally attributed to pickup He^+ but are instead strongly suggestive of an energized H^+ source. These latter events show wave signatures peaking close to the H^+ cyclotron frequency and diminishing at frequencies approaching the He^+ cyclotron frequency.

Figure 2 shows the average ambient plasma parameters for the intervals studied here. The left column shows the control intervals (black squares) and collective wave events due to pickup He^+ (red triangles). The right column shows the parameters associated with the strong He^+-associated wave events (green circles) and the observations that suggest association with energized H^+ (blue plusses). There is no clear distinction between the ambient plasma conditions of weak and strong wave events. The mean magnetic field intensity B and angle between the mean field and the radial direction Θ_{BR} are computed using the high-cadence FGM data. The instabilities employed here rely on particle streaming greater than the Alfvén speed. Although there are a few instances of waves observed with $\Theta_{BR} \simeq 90°$, almost all wave observations are at sufficiently small values of Θ_{BR} to allow for the instabilities to operate. The remaining average ambient plasma parameters employ the thermal ion data, which have a lower cadence than the FGM data and are generally slower to change. For

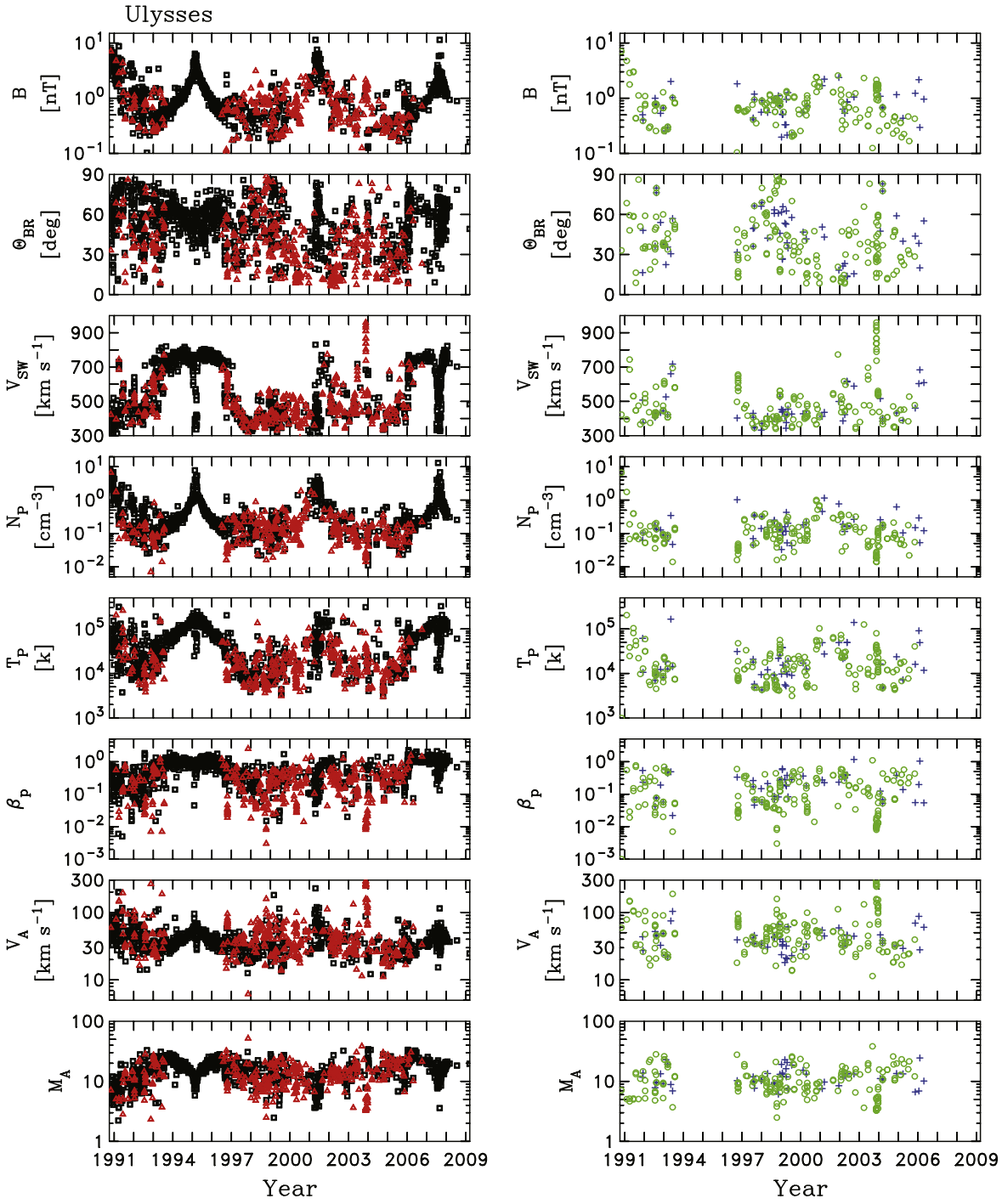

Figure 2. Ambient plasma parameters for the times studied here. (left column) Wave and control intervals are again represented by red triangles and black squares, respectively. (top to bottom) We plot the average magnetic field intensity B in nT, the angle between the mean field and the radial direction Θ_{BR} in degrees, the mean solar wind speed V_{SW} in units of km s^{-1}, the thermal proton density N_P in units of cm^{-3}, the thermal proton density T_P in units of Kelvin, the proton energy density parameter β_P, the Alfvén speed V_A in units of km s^{-1}, and the Alfvén Mach number M_A. (right column) Same for wave intervals with $|E_{lip}| \geqslant 0.35$ (green circles) and intervals showing evidence of possible H^+ acceleration (blue plusses).

parameters using SWOOPS data, we averaged the merged hourly data from the two instruments. The average magnetic field intensity, wind speed, thermal proton density, and proton temperature are straightforward averages of the data. The angle Θ_{BR} is computed from the mean magnetic field vector. Likewise, the mean parameters are used to compute the Alfvén speed V_A, the Alfvén Mach number M_A, and $\beta_P = 8\pi N_P k_B T_P / B^2$, where k_B is Boltzmann's constant. Using the measured variables in the units described, we can write $\beta_P = 3.47 \times 10^{-5} N_P T_P / B^2$ and $V_A = 21.8 B N_P^{1/2}$.

A comparison of Figures 1 and 2 shows some interesting features. The value of B is at a minimum when $R \simeq 5$ au and at a maximum at the near-ecliptic center of the fast latitude scan. The variation seen in B, N_P, and T_P as Ulysses moves from apoapsis to periapsis comes from the combined effects of heliodistance and heliolatitude. The parameters V_A and M_A, as well as the wind

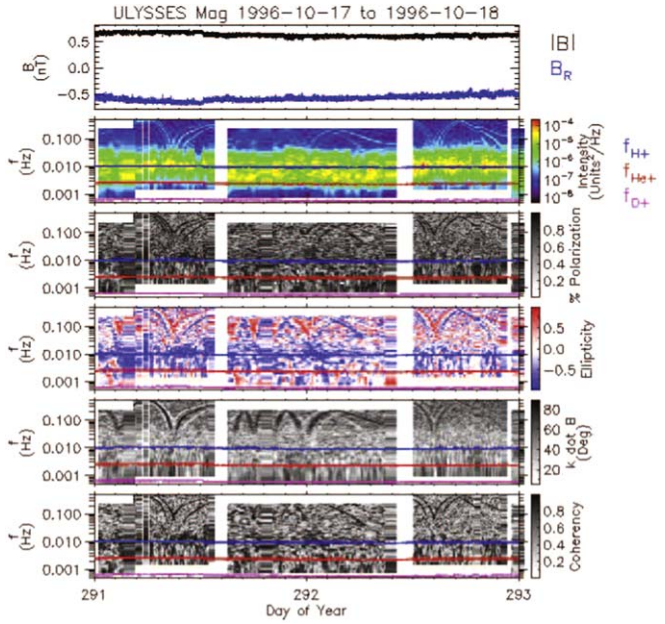

Figure 3. Example of the daily spectrograms used to locate the wave events studied here. The data analyzed are DOYs 291–292 of 1996 when the spacecraft was at 4.46 au, a heliolatitude of 24°.2, and a heliolongitude of 76°.6. The spectrogram shows (top to bottom) the time series for B and B_R in heliocentric (R, T, N) coordinates. The second panel shows the power spectrum followed by the degree of polarization. Next is the ellipticity and then the angle between the minimum variance direction and the mean magnetic field. The last panel is the coherence. Horizontal lines represent the cyclotron frequency of H^+, He^+, and O^+.

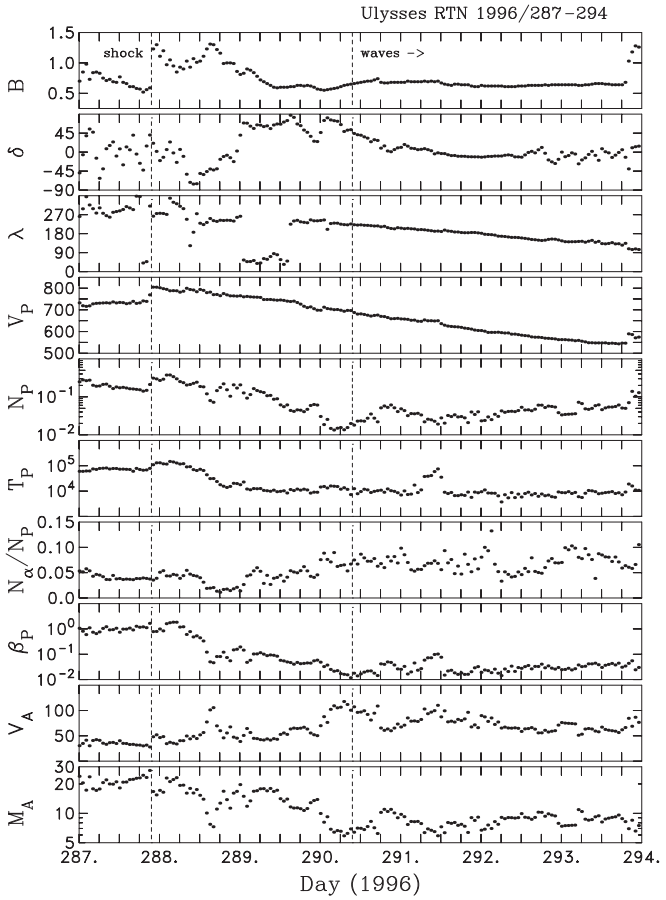

Figure 4. Time series plot of the magnetic field and thermal ion data for 1996 DOYs 286–293. The waves are seen well into a rarefaction interval lasting six days.

speed V_{SW}, show the established signature of high-latitude solar minimum conditions that is less significant during the 2001 pass. The parameter β_P also varies with distance and latitude but not as strongly as some other parameters. It is noteworthy that very few data intervals exhibiting waves due to pickup He^+ exist within the two fast latitude scans that occur during the solar minimum.

2.2. Spectral Analysis

We use a combination of spectral analysis techniques to identify and analyze relevant data intervals. The highest resolution FGM data were downloaded as daily files and used to produce automated spectrograms via standard Fast Fourier Transform (FFT) techniques (Fowler et al. 1967; Rankin & Kurtz 1970; Means 1972; Mish et al. 1982; Argall et al. 2015, 2017; Fisher et al. 2016; Hollick et al. 2018a). Figure 3 is an example of those spectrograms using magnetic field data from DOYs 291–292 of 1996. It shows (top to bottom) the time series for B and B_R in heliocentric (R, T, N) coordinates, where R is directed from the Sun to the point of the measurement, T is coplanar with the Sun's rotational equator and directed in the sense of rotations, and $N = R \times T$. The second panel shows the power spectrum followed by the degree of polarization. Next is the ellipticity, which carries the sign of the polarization followed by the angle between the minimum variance direction and the mean magnetic field for that subinterval used to compute the spectrum. The last panel is the coherence. Horizontal lines represent the cyclotron frequency of H^+, He^+, and O^+ (top to bottom). Note that the cadence of the magnetic field data changes during the two days shown, which is typical of the Ulysses data, thereby changing the Nyquist frequency. Gaps occur where the changing measurement cadence renders the spectrum uncomputed.

Because the power spectrum covers an extended range of values and enhancements due to PUIs are generally small, examination of these spectrograms seldom leads to finding waves due to PUIs. The most reliable way to find waves due to PUIs is to examine the ellipticity plot for bands of uniform color. They can be found throughout much of these two days at the cyclotron frequencies associated with H^+ and He^+. If particle energization is not present, as it is expected not to be for most of the wave observations, the enhancement in the ellipticity will be seen at spacecraft frame frequencies $f_{sc} \geqslant f_{i,c}$. There should be a hard cutoff of any wave signatures at $f_{sc} < f_{i,c}$. The ellipticity enhancements seen are largely in the range $f_{He,c} < f_{sc} < f_{p,c}$ leading us to conclude that these waves are likely due to pickup He^+. However, close examination of the spectra when computed with more deliberate care shows that there are wave signatures in the range $f_{pc} < f_{sc} < 2f_{p,c}$ that are either due to pickup H^+ or scattered He^+. One way to address this uncertainty will be to compare the growth rate for waves due to newborn interstellar pickup H^+ to the turbulence rate to see if this source is likely to produce wave growth.

Once likely intervals of enhanced wave activity are found using the automated techniques, we make careful analysis of select time intervals using a combination of prewhitened Blackman–Tukey analysis of the power spectra (Blackman & Tukey 1958; Matthaeus & Goldstein 1982; Chen 1989; Smith et al. 1990, 2006a, 2006c; Leamon et al. 1998a, 1998b; Hamilton et al. 2008; Markovskii et al. 2008, 2015) and FFT analysis of the polarization spectra (Fowler et al. 1967; Rankin & Kurtz 1970;

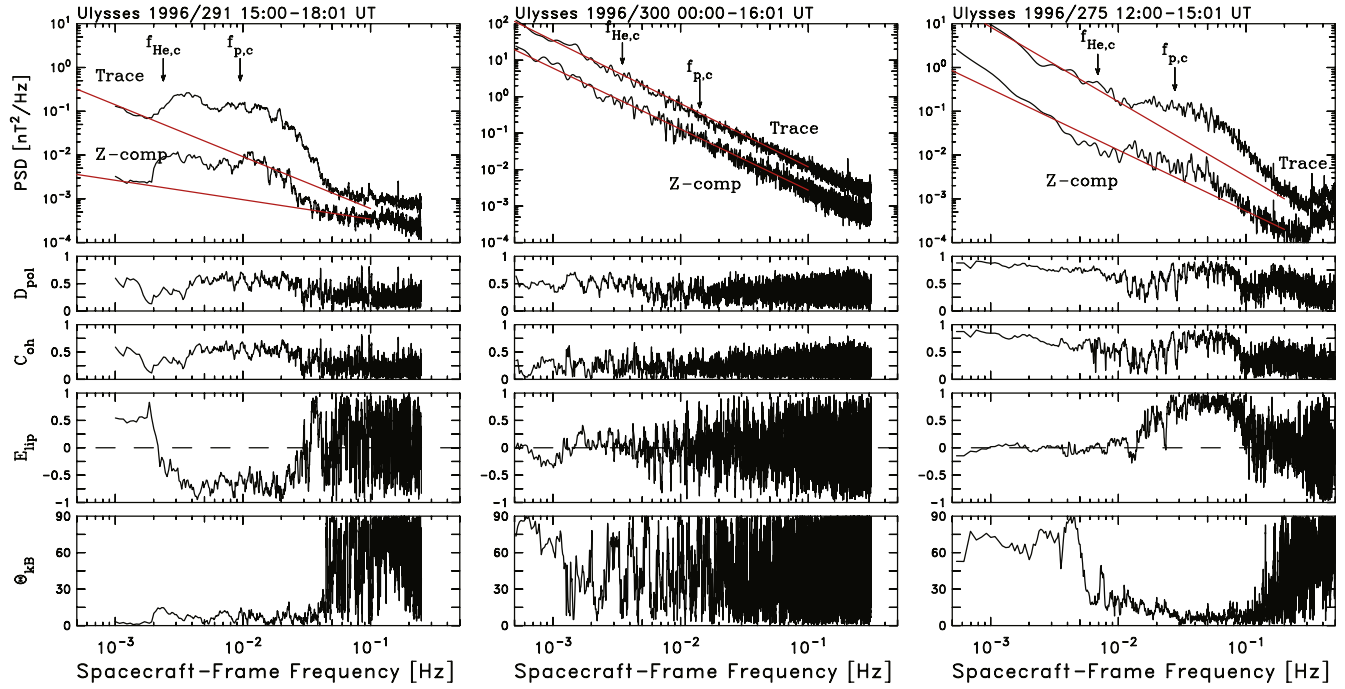

Figure 5. Examples of spectra used in this study. (left) Wave interval arising from pickup He^+ on DOY 291 of 1996. (middle) Control interval dominated by turbulence dynamics on DOY 300 of 1996. (right) Example of spectra showing possible energization of pickup H^+ population on DOY 275 of 1996.

Means 1972; Mish et al. 1982). These are the same techniques used previously to study magnetic waves due to interstellar pickup ions in the ACE and Voyager data sets (Joyce et al. 2010, 2012; Cannon et al. 2014a; Argall et al. 2015, 2017; Aggarwal et al. 2016; Fisher et al. 2016; Hollick et al. 2018a).

One-minute FGM data were downloaded and used to create 10 day time series plots of the FGM data for reference when selecting time intervals that are suitably homogeneous and free of large, isolated discontinuities. Merged hourly data were then plotted to obtain a better understanding of large-scale dynamics such as shocks. The time series plots have proven very useful in identifying possible alternate sources for the waves found via the spectrograms.

Figure 4 shows a plot of the combined Ulysses FGM and SWOOPS data for DOYs 287–293 of 1996, which includes the two days shown in the spectrogram above. The panels are (top to bottom) the magnetic field strength B in nT, elevation angle in degrees, clock angle in the (R, T) plane where 0° points radially away from the Sun, wind speed V_P in km s^{-1}, solar wind proton density N_P in cm^{-3}, solar wind proton temperature T_P in K, ratio of alpha particle to proton densities, thermal proton beta, Alfvén speed in km s^{-1} computed from the thermal protons, and Alfvén Mach number of the flow. A shock is evident on DOY 287.9 and marked by a vertical dashed line followed by a coronal mass ejection and magnetic cloud that extends until the start of DOY 289. The waves in question are first observed midday on DOY 290 with the onset marked by the second vertical dashed line and continue until ∼06:00 UT on DOY 293. By this time, the flow is within an expansion region of decreasing wind speed and density that extends until the last few hours of DOY 293. It is not uncommon to find waves due to newborn interstellar PUIs within rarefaction regions because the turbulence is weak there. We have analyzed this wave interval in several smaller subsets because (1) the cadence of the data changes repeatedly during this time and (2) the relative strength of waves associated with He^+ and H^+ varies.

Figure 5 shows the polarization analysis for three data intervals that represent the different types of observations reported here. Figure 5 (left) shows our analysis of hours 15:00–18:01 UT on DOY 291 of 1996. This is a subset of the wave observations seen in Figure 3 under the solar wind conditions show in Figure 4. The analysis of the power spectra (top panel) is performed using the Blackman–Tukey technique where the spectrum is derived from the Fourier Transform of the autocorrelation function. The polarization analysis is performed using the technique of Fourier transforming the time series. The top panel shows the trace of the power spectral matrix and the spectrum of the field-aligned fluctuations (Z-comp). The fit lines are determined to represent the background power spectra apart from the enhanced wave energy. The panels below the power spectra are the spectra of the degree of polarization $0 \leqslant D_{\rm pol} \leqslant 1$, coherence $0 \leqslant C_{\rm oh} \leqslant 1$, ellipticity $-1 \leqslant E_{\rm lip} \leqslant 1$, and the angle between the minimum variance direction and the mean magnetic field $0° \leqslant \Theta_{kB} \leqslant 90°$.

The power spectra in Figure 5 (left) show two significant results. First, there is a large enhancement in the power relative to the background spectra (red lines) at frequencies $f_{\rm sc} \geqslant f_{{\rm He},c}$ indicative of excitation by pickup He^+ and probably pickup H^+ as well. Second, the total power exceeds the power in the parallel component by a factor of ∼10. This indicates that the fluctuations are transverse to the mean magnetic field and therefore noncompressive as is expected from the theory (Lee & Ip 1987). Both $D_{\rm pol}$ and $C_{\rm oh}$ are elevated at $f_{{\rm He},c} \leqslant f_{\rm sc} \leqslant$ 0.03 Hz, coninciding with the enhanced power. This same frequency range shows $E_{\rm lip} \simeq -1$, which indicates the fluctuations are left-hand polarized in the spacecraft frame. Again, this is expected from the theory. The normal undisturbed solar wind spectrum is unpolarized at these frequencies with lower values of $D_{\rm pol}$ and $C_{\rm oh}$. Last, and in keeping with the power spectra, the minimum variance direction is aligned with the mean magnetic field. There are small, suggestive features in the

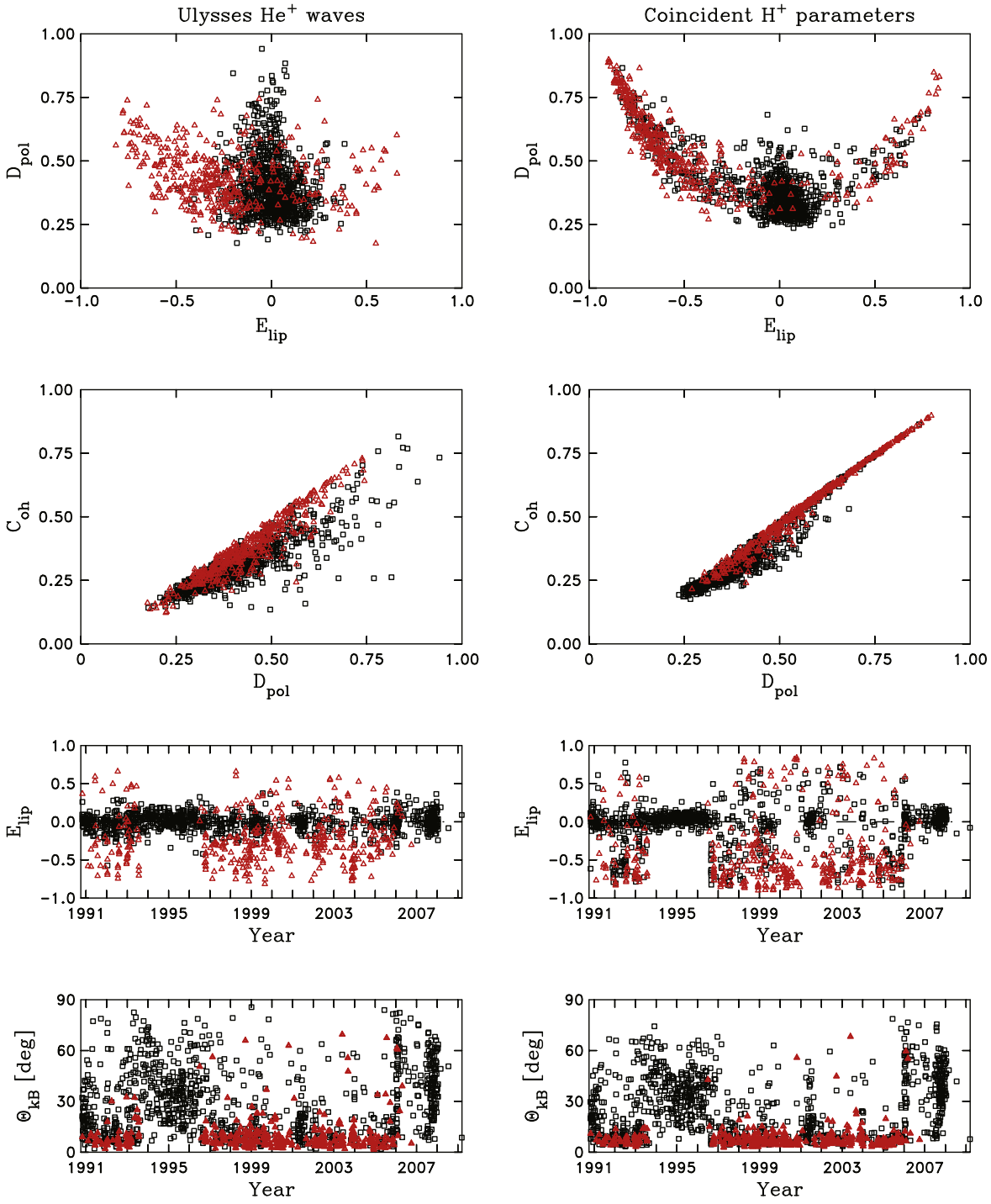

Figure 6. Polarization parameters for the frequency range $f_{\mathrm{He},c} < f_{sc} < 2f_{\mathrm{He},c}$ (left) and $f_{p,c} < f_{sc} < 2f_{p,c}$ (right). Red triangles denote times when waves due to pickup He^+ are seen, and this includes the panels on the right. Black squares denote times when waves due to pickup He^+ are not seen. It can clearly be observed on the right that there are data intervals with high values of $|E_{\mathrm{lip}}|$ and D_{pol} when waves due to pickup H^+ are present, but without the waves associated with He^+.

spectra, and most notably E_{lip}, that suggests separate He^+ and H^+ sources, but these are not strong or statistically significant. Using the analysis methods described below, the ratio of the wave growth rate due to the pickup He^+ (H^+) to the turbulence rate is 47 (15) indicating that the local dynamics are dominated by wave growth and the turbulence is too weak to prevent the accumulation of wave energy. We should note that there are weak shock candidates late on DOY 287 and again late on DOY 293. However, there is no evidence of He^+ ions accelerated beyond the pickup energy and we believe that wave observations during this interval and others nearby are the result of pickup dynamics.

Figure 5 (middle) shows our analysis of a control interval 00:00–16:01 UT on DOY 300 of 1996. This occurs within a stream interaction region when the wind speed exceeds 700 km s^{-1}. There is no evidence of waves due to pickup ions, either He^+ or H^+, or any other suprathermal population at this time. There is no enhancement of the wave energy spectrum at the associated cyclotron frequencies, no increase in D_{pol} or C_{oh}, no bias of E_{lip}, and no alignment of the minimum variance direction

with the mean field direction at the associated cyclotron frequencies. The ratio of the wave growth rate due to pickup He^+ (H^+) to the turbulence rate is 4.4×10^{-3} (4.8×10^{-2}). This indicates that the turbulence is too strong to permit the wave energy to accumulate. We should note that there appears to be several shocks candidates in the general vicinity of the measurement. There is a shock late on DOY 293, another late on DOY 297, and a third late on DOY 301. Although we have not analyzed these possible shocks, the significant fact is that there is no evidence of waves due to suprathermal particles of any source during the time in question.

Figure 5 (right) shows an example from DOY 275 of 1996 where wave energy and polarization that may possibly be associated with pickup H^+ extends to frequencies below $f_{p,c}$. Supporting this interpretation, we find that the ratio of the wave growth rate for pickup He^+ (H^+) to the turbulence rate is 0.14 (2.6), which would appear to make a pickup He^+ source unlikely. This suggests that any wave energy seen is the result of suprathermal H^+ alone. The form of the spectrum supports this interpretation and indicates energization of H^+ by some means. Pickup He^+ with an initial pitch angle of 0° will excite waves at $f_{sc} = f_{He,c}$. It is the scattered He^+ ions that produce wave growth near the proton cyclotron frequency. So either the scattering of He^+ is somehow disrupted or the H^+ ions are energized beyond the initial pickup energy to yield the wave energy at $f_{sc} < f_{p,c}$. Resolution of this question lies outside the realm of this paper, but we should note that this time interval is within a stream interaction region with a possible weak shock candidate late on DOYs 274 and a stronger candidate on DOY 277. So, this observation may be the result of shock acceleration. The alignment of the minimum variance direction with the mean field direction does extend down to $f_{He,c}$, but this is often seen in cases of solar wind turbulence.

In order to characterize the polarization parameters associated with wave excitation by pickup He^+, we average the polarization spectra over the range $f_{He,c} \leqslant f_{sc} \leqslant 2f_{He,c}$. We limit the range in this way with the intent of excluding any waves at higher frequencies arising from a H^+ source. At the same time, we examine every polarization spectrum and independently (and subjectively) characterize each event as showing or not showing evidence of wave excitation by pickup He^+. That characterization is based upon the spectra of the three polarization parameters, the minimum variance direction, and the fluctuation power. Evidence of wave excitation is sometimes seen in parameters other than E_{lip}.

Figure 6 (left column) shows the distribution of polarization parameters at He^+ frequencies. Again, the intervals characterized as exhibiting waves are shown as red triangles, while the remaining intervals are shown as black squares. The top left panel shows the D_{pol} average plotted as a function of E_{lip} and shows behavior similar to related plots by Hollick et al. (2018a). Note the presence of right-hand polarized waves. This has been seen in both ACE (Fisher et al. 2016) and Voyager (Hollick et al. 2018a) observations of waves due to pickup He^+ as well as Ulysses observations of waves due to pickup H^+ (Cannon et al. 2014a). There is a central cluster of control intervals that form a large black triangular structure. The wave events (red symbols) are normally seen as two wings at $|E_{lip}| > 0.35$, but here we see what we have judged to be examples of wave excitation at He^+ frequencies with low values of $|E_{lip}|$. These are the events where there is significant bias in E_{lip} or elevation of D_{pol} and C_{oh} or sometimes enhancement in the power within the range $f_{He,c} < f_{sc} < f_{p,c}$, but which may not be a strong signature or may not extend significantly to $f_{He,c}$. In past analyses, we were more conservative and did not consider such observations as wave events, but here we see them in greater abundance and seek to address them.

Continuing down the left side of Figure 6, we see the familiar correlation between D_{pol} and C_{oh}, where the waves show a tighter correlation than the controls. Below that, there is a plot of E_{lip} as a function of time (in years), showing again that the wave events are generally seen throughout the lifetime of the mission except during the fast latitude scans of the solar minima. It is further evident that the strongly polarized $E_{lip} < -0.35$ waves exist throughout the times when waves are observed generally and are not isolated to any particular subset of the orbit. The bottom left panel shows Θ_{kB} plotted as a function of time (in years). Although there are a scattered wave events with $\Theta_{kB} > 15°$, most have minimum variance directions that are approximately field-aligned. This is expected from the theory (Lee & Ip 1987), as the resonant beam instability is strongest for field-aligned wavevectors. Control intervals show a greater range of Θ_{kB} values that appears to be maximum during the fast latitude scans.

The right column of Figure 6 shows the polarization parameters computed over the frequency range $f_{p,c} \leqslant f_{sc} \leqslant 2f_{p,c}$, but we retain the color convention that red triangles signify wave activity at He^+ frequencies. In other words, these are the fluctuation parameters associated with H^+ frequencies during times of He^+-associated waves and their controls. The analysis of waves due to H^+ has already been performed (Cannon et al. 2013, 2014a, 2014b, 2017). The top right panel shows the two horns of the distribution at $|E_{lip}| > 0.35$ that we have come to expect. However, note that some of those intervals are controls in this analysis in that there is no evidence of waves due to He^+, while this is clear evidence of waves due to pickup H^+. There are also times when waves are seen due to He^+, while waves due to H^+ are not observed. This is most notable inside $R = 3.5$ au, because neutral H does not penetrate as deeply into the heliosphere as does neutral He. There are times when He^+ events have low values of $|E_{lip}|$ at H^+ frequencies, but many other times when the two wave sources are seen to be coincident in the spectra. This raises the question of whether intervals with less compelling values of E_{lip} at He^+ frequencies can be attributed to energization of the H^+ population, or to inefficient or incomplete scattering of the He^+ ions. We cannot answer this question here.

The remainder of Figure 6 is as expected. There is a strong correlation between D_{pol} and C_{oh} as well as an absence of high $|E_{lip}|$ events during the fast latitude scans of solar minima. Minimum variance directions at H^+ frequencies associated with He^+ events tend to be field-aligned. This could be due to wave excitation by H^+ or high-frequency wave excitation by He^+.

Figure 7 plots E_{lip} averaged over the range of He^+ frequencies $f_{He,c} \leqslant f_{sc} \leqslant 2f_{He,c}$ as a function of Θ_{BR}. The idea of newly ionized pickup ions streaming sunward is based upon the simple model of a radial mean magnetic field. While elevated values of $|E_{lip}|$ do favor lower values of Θ_{BR}, in so far as there are more He^+ wave events at lower values of Θ_{BR}, there are also a significant number of events at higher values of Θ_{BR}. The preference for lower values of Θ_{BR} may reflect a reduced turbulence level in rarefaction intervals so that the field orientation is more coincidental than a necessary element of the instability.

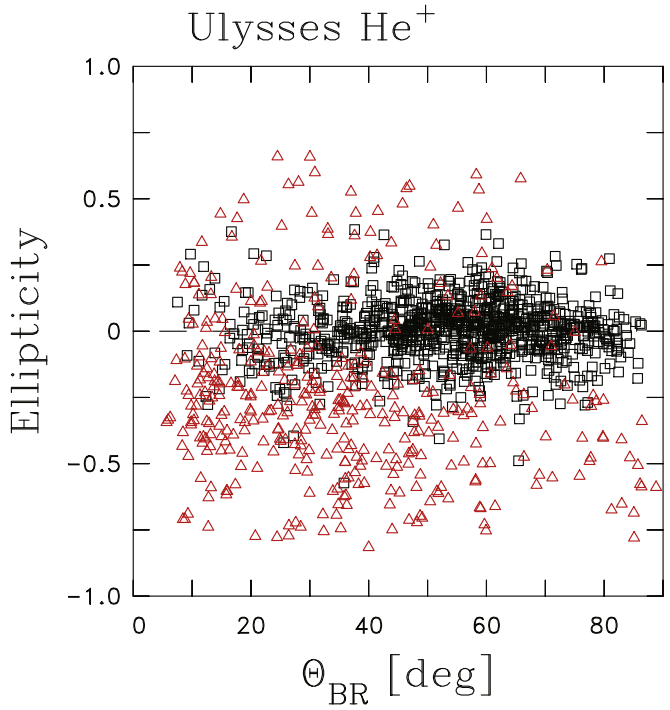

Figure 7. Scatter plot of the ellipticity at resonant He^+ frequencies for control intervals and wave events plotted as a function of Θ_{BR}. Note that the wave events do tend to have larger ellipticities but also show a greater concentration at smaller values of Θ_{BR}.

Figure 8 (top) shows the location of our identified He^+-excited wave events. Latitudes $\simeq 0°$ show a series of events as Ulysses made its way to Jupiter before entering the high-latitude orbit that followed passage of the spacecraft over the Jovian poles. There is a greater density of wave events at the more distant part of the orbit, but it should be noted that the spacecraft is moving more slowly at this point. Although not as numerous, there are wave events at high latitude $|\Theta_{\rm lat}| > 60°$. Figure 8 (bottom) shows the location of our identified He^+-excited wave events with $|E_{\rm lip}| > 0.35$. This reduces the wave ensemble to 180 data intervals. Although the four wave events identified during the fast latitude scans are here seen to have $|E_{\rm lip}| < 0.35$ and are not evident in the bottom panel, there is no significant evidence that the intervals with high or low values of $|E_{\rm lip}|$ exist only within a limited segment of the Ulysses orbit. Limiting the analysis to $|E_{\rm lip}| > 0.35$ does not preferentially remove the high-latitude observations or the more distant observations.

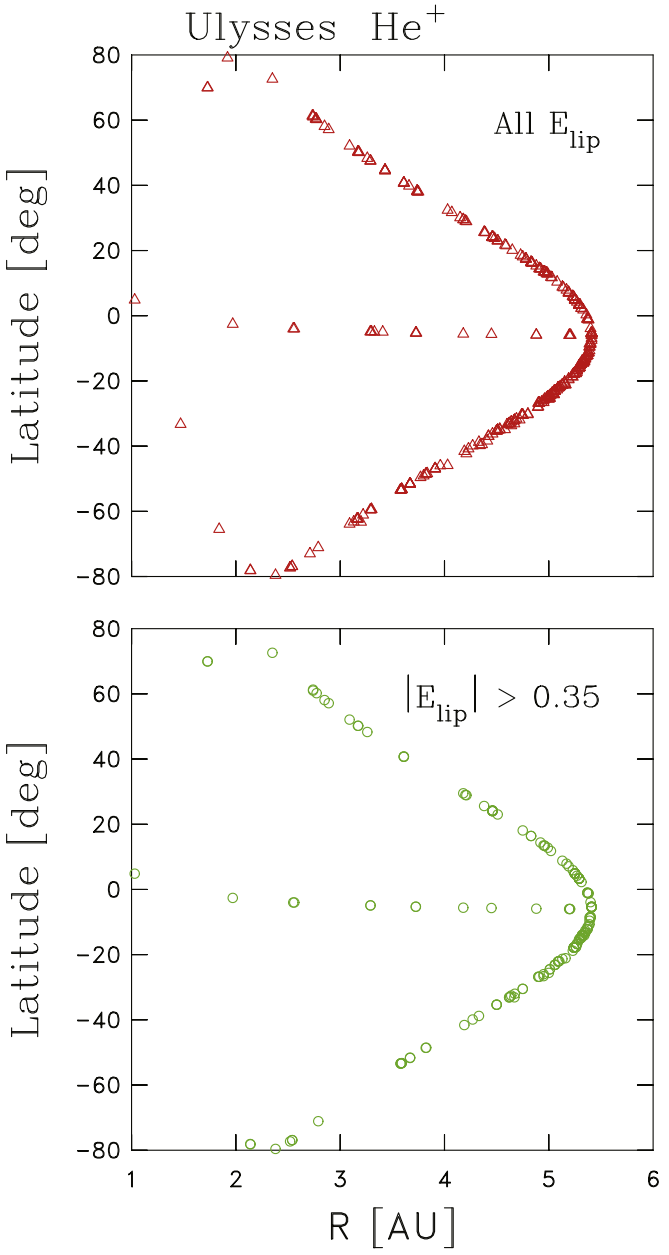

Figure 8. Location of He^+-excited wave events along the Ulysses trajectory. (top) Location of all intervals that are identified as He^+ events. (bottom) Location of all identified He^+ events with $|E_{\rm lip}| > 0.35$.

3. Wave Excitation and Turbulence Rates

Past studies have shown that the slow accumulation of wave energy excited by the scattering of newborn interstellar PUIs is readily overwhelmed by the background turbulence. This turbulence absorbs the wave energy and remakes it into forms that are dictated by the nonlinear dynamics (Cannon et al. 2014b; Hollick et al. 2018b; Pine et al. 2020). It then transports this energy to smaller scales where dissipation heats the background plasma. However, there are times when the turbulence is weak, and at these times it becomes possible for the wave energy to accumulate to observable levels. This process requires hours and is long compared to the time required to scatter individual ions, so we postulate that the slow accumulation of scattered ions and associated wave energy passes through a sequence of quasi-stationary, asymptotic states as predicted by Lee & Ip (1987). Our approach is to compute numerically the derivative of the asymptotic theory, since PUIs accumulate at a known rate that is predicted from theory and modeling.

3.1. Neutral Atom Ionization

To calculate the interstellar neutral species densities and PUI production rate, we used the nWTPM code (for a detailed description, see Tarnopolski & Bzowski 2009 for H and Sokół et al. 2015 for the species insensitive to the solar radiation pressure: He, Ne, O). The WTPM code calculates the density and higher moments of the distribution function of interstellar neutral (ISN) gas. It uses the hot model paradigm (Fahr 1978, 1979) extended to account for heliolatitude and time

variations of the ionization losses of ISN atoms inside the heliosphere, and for the time- and radial-speed-dependent radiation pressure force.

In the calculation of the densities, we used the model of ionization factors (charge exchange between solar wind protons and alpha particles, photoionization, and electron impact) from Sokół et al. (2020). For radiation pressure, we used a model of evolution of the spectral shape of the solar Lyα line by Kowalska-Leszczynska et al. (2020). Even though the models of the ionization factors and radiation pressure are based on measurement time series obtained at 1 au, we did not apply any delay in the calculation of ISN gas densities away from 1 au because the time resolution of these two models (the Carrington rotation period, ~27.4 days) is comparable to the time delay between 1 au and Ulysses aphelion, located at the orbit of Jupiter.

Calculation of the PUI production rates at the sites of Ulysses measurements requires knowledge of the local ionization environment, in particular of the solar wind parameters. These parameters are typically obtained from Ulysses on-board measurements. In situ plasma measurements were unavailable for 14 intervals from the in-ecliptic cruise, which occurred during the first 22 days we studied. In these instances, and only these instances, we applied a similar procedure to that used recently for the analysis of Juno measurements: we estimated the solar wind parameters at Ulysses based on the OMNI2 data product (King & Papitashvili 2005). OMNI2 has solar wind measurements performed at Earth by various space experiments, appropriately adjusted to a common calibration. Since these data are available for the Earth location in time and space, and we need them at Ulysses, the OMNI solar wind parameters had to be adapted to account for the finite travel time of the solar wind between 1 au and Ulysses and the difference in the longitude. This could only be done in an approximate way.

This approximate procedure to calculate the 14 intervals of solar wind proton, electron, and alpha densities and speeds at Ulysses was iterative. For a time t_1, the time of a measurement at Ulysses, the solar wind speed $V_{SW,1}$ from the OMNI2 collection averaged over the Carrington rotations was selected. With this, we calculated $t_{start} = t_1 - \Delta R/V_{SW,1} - 90$ days, where ΔR is the difference between the Earth's and Ulysses distances to the Sun. The 90 days were subtracted to make sure that the initial guess time t_{start} was early enough.

Starting from $t_i = t_{start}$ and increasing t_i by 1 day in each iteration, we calculated $V_{SW,i}(t_i)$ by linear interpolation of the Carrington period-averaged OMNI2 time series. With this, we calculated $t_2 = t_i + \Delta R/V_{SW,i}$. If the t_2 thus obtained is within 1 day of t_1, the pair (t_i, $V_{SW,i}$) is stored. Otherwise, the next iteration is performed. Along with the solar wind speed, the proton n_{pi}, α n_α, and electron densities n_{ei} are also calculated. To obtain the solar wind parameters needed to calculate the production rates of PUI at Ulysses, the series ($V_{SW,i}$, n_{pi}, $n_{\alpha i}$, n_{ei}) are averaged, and the resulting quantities are used in the formulae for the charge exchange and electron impact rates. For the rates of PUI production by photoionization, we used directly the Carrington-averaged photoionization rates from Sokół et al. (2020) interpolated to the time of Ulysses measurements.

For all locations in the Ulysses orbit that we use either as wave events or controls, we calculated the ISN densities using our standard procedure, and in the calculation of the PUI production rates, measurements of the solar wind parameters available directly from Ulysses instruments were used. Figure 9 shows the result of that analysis. Both the per neutral ionization rate and the ion production rate for He^+ are shown. There is a strong variation associated with heliocentric distance as is expected for an ionization process based on the intensity of solar EUV radiation. Closer inspection will reveal a solar cycle dependence as represented by a slight flattening of the ionization curve during the rising phase from 1997 to 2001. In addition to serving as input for the theory of wave excitation, this result demonstrates the low degree of variability for He^+ production. There is clearly significant variation in time and space across the orbit, but neighboring wave events and control events do not show significant variation. This gives further evidence to the claim that observability is based on the more highly variable turbulence rate than on variations in ion production.

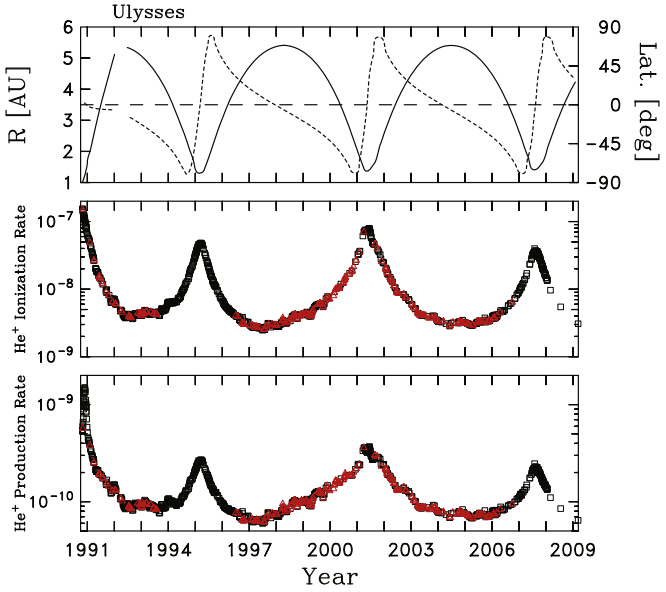

Figure 9. (top) Trajectory of the Ulysses spacecraft reproduced from Figure 1. (middle) He^+ per neutral ionization rates in units of s^{-1}. This represents the likelihood of an individual neutral He atom being ionized at this point in time and space. (bottom) He^+ production rate in units of $cm^{-3}\ s^{-1}$ is the product of the neutral He atom density and the He^+ ionization rate. This is the actual rate of He^+ production for each time interval in the study.

3.2. Wave Excitation

We calculate our growth rates for waves excited by new interstellar H^+ and He^+ using measurement units as provided by the instrument teams: $\boldsymbol{B}$ [nT], V_{SW} [km s^{-1}], N_P [cm^{-3}]. The formula derived by Lee & Ip (1987) for the time-asymptotic wave spectrum, which assumes full scattering of PUIs, is given by

$$I_{\pm}(k, \infty) = \frac{1}{2}[C(k)^2 + 4I_+(k, 0)I_-(k, 0)]^{1/2} \pm \frac{1}{2}C(k), \quad (1)$$

where the background spectrum at wavenumber k for fluctuations at time equal to zero is $I_+(k, 0)$ when propagating anti-sunward, and $I_-(k, 0)$ when propagating sunward. This produces spectra with units [nT^2 km]. Summing over the four permutations of Equation (1) (i.e., $I_{tot}(k, \infty) = I_+(+k, \infty) + I_+(-k, \infty) + I_-(+k, \infty) + I_-(-k, \infty)$) gives the entire spectrum. Negative k represents right-hand polarized fast-mode waves, and positive k represents left-hand polarized Alfvén waves for sunward propagating waves. Because the only waves considered are those

propagating parallel to the magnetic field, the theory is one-dimensional. The wave enhancement term is

$$C(k) = I_+(k, 0) - I_-(k, 0) + 2\pi m_i n_i V_A |\Omega_{i,c}| k^{-2} \times \left[\Omega_{i,c} k^{-1} v_0^{-1} - \frac{(\Omega_{i,c} k^{-1} v_0^{-1} - \mu_0)}{|\Omega_{i,c} k^{-1} v_0^{-1} - \mu_0|} \right], \quad (2)$$

where m_i is the pickup ion mass, n_i is the pickup ion number density, V_A is the Alfvén speed, v_0 is the PUI speed in the plasma frame, μ_0 is the pitch angle of the new pickup ions, v_0 is taken to be equal to the solar wind speed V_{SW}, and $\Omega_{i,c} = 2\pi f_{i,c}$, with $f_{i,c} = e_i B/(2\pi m_i c)$ being the ion cyclotron frequency. In this term, e_i is the charge of the pickup ion, B is the local magnetic field intensity, and c is the speed of light. We assume that the background turbulent spectrum in Equation (2) can be described as $I_+(k, 0) = I_-(k, 0) = (1/4) I_{tot}(k_{i,c}, 0) k^{-5/3}$, where $I_{tot}(k_{i,c}, 0) = I_+(+k_{i,c}, 0) + I_-(+k_{i,c}, 0) + I_+(-k_{i,c}, 0) + I_-(-k_{i,c}, 0)$ is the total background intensity at the ion cyclotron frequency. The wavenumber of the PUI at zero pitch angle is $|k_{i,c}| = 2\pi f_{i,c}/V_{SW}$. This methodology was originally used by Cannon et al. (2014b), based on techniques from Joyce et al. (2010).

By assuming that the PUI production rate is slow compared to their subsequent scattering, we can use these formulas to evaluate the growth in the wave energy as PUI density increases. This is under the assumption that the wave spectrum passes through a sequence of asymptotic forms as the PUI density increases. This was done in Joyce et al. (2010) by multiplying the production rate of new PUIs by an artificial accumulation time. The accumulation time was varied such that the resulting spectrum would match the observation. That product was compared to the computed timescale for turbulent destruction of waves. In Cannon et al. (2014b) and Hollick et al. (2018b), this procedure was modified so that the total wave power was computed at the peak of the spectrum associated with wave excitation at two different accumulation times, and the differential was used to find wave growth rates. This is the method we use here.

Energy in the wave spectrum, caused by ion cyclotron resonance with the PUI population, accumulates at a rate of

$$\frac{dE_W}{dt} = R_{ac} \times 10^{10} \times 10^{-5} \times \left(\frac{2\pi f_w}{V_{SW}} \right) \left(\frac{21.8^2}{N_P} \right) \cdot \frac{1}{3600}. \quad (3)$$

There are several unit conversion factors in Equation (3) that we call out explicitly. The factor 21.8 converts the magnetic field to Alfvén speed units, 10^{10} converts Gauss^2 to nT^2, and 10^{-5} converts cm to km. The spacecraft-frame frequency is f_w where the wave power peaks. The solar wind speed V_{SW} is in km s^{-1}, and N_P is in cm^{-3}. The accumulation rate R_{ac} is given by $[I_{peak}(t_{acc2}) - I_{peak}(t_{acc1})]/[t_{acc2} - t_{acc1}]$. In this, t_{acc2} and t_{acc1} are two different accumulation times, and $I_{peak}(t_{acc})$ is $I_{tot}(k, \infty)$ evaluated at the peak of the wave enhancement using n_i equal to t_{acc} times the newborn PUI production rate. The minimum acceleration that produces a wave enhancement in the computed wave spectrum (the local maximum) is t_{acc1}, and $t_{acc2} = t_{acc1} + 20$ hr. We have tried values other than 20 hr and find that most computed growth rates vary by only ~20% with very few examples varying by a factor of 2. This small variation does not alter the conclusions of the paper. Wave growth rates for He$^+$ and H$^+$ are computed independently. Thus, we assume that wave excitation by pickup He$^+$ has no effect on the wave spectra used to compute the growth rates for pickup H$^+$, and vice versa.

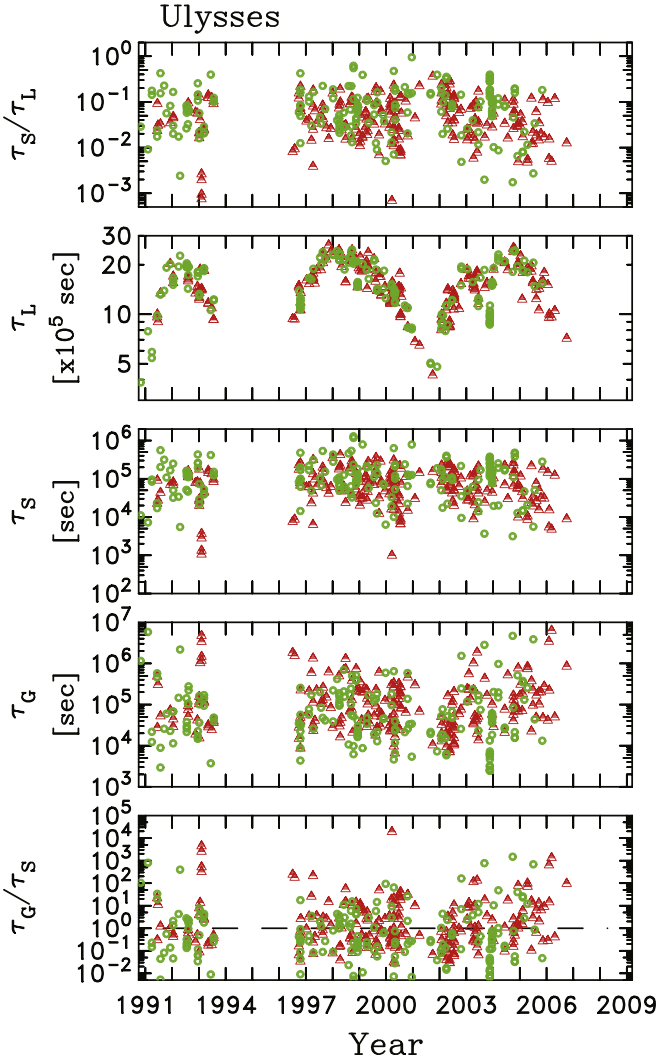

Figure 10. Comparison of timescales for the pickup He$^+$ scattering problem. Red triangles with the upper half filled in represent wave events with $|E_{lip}| < 0.35$. (top to bottom) Ratio of the time required to scatter a PUI through 180°, τ_S, to the lifetime of the solar wind (convection time from the Sun to the point of observation), τ_L; the lifetime and scattering time shown separately; the growth time for the waves, τ_G, to reach the background power level at $f_{sc} = f_{He,c}$; and the ratio of the growth time to the PUI scattering time.

The assumption on which our theory analysis is based is that the pickup He$^+$ population is scattered and maintains an asymptotic form as newly ionized particles contribute to wave growth. It is therefore desirable that the scattering time be short compared to the wave growth time. Figure 10 shows our analysis of, $\tau_L = R/V_{SW}$, the lifetime of the plasma (the convection time from the Sun to the point of observation); the time required to scatter a pickup He$^+$ through 180°, τ_S; and the time required to grow the wave to the level of the background spectrum at $f_{sc} = f_{He,c}$ using the computed wave energy growth rate described above. Following Lee & Ip (1987), we compute $1/\tau_S = (9/110)\Omega^2 I(k = 2\pi f_{He,c}/V_{SW})/B^2$, where $I(k = 2\pi f_{He,c}/V_{SW})$ is the measured background power spectrum in units of nT^2 km. The local scattering time is smaller than the lifetime of the plasma

with most events falling in the range $10^{-2} < \tau_S/\tau_L < 0.5$. The plot of τ_L shows the expected convection time dependence upon heliocentric distance. Comparison against the plot of τ_S/τ_L demonstrates that τ_S must follow a similar dependence. Therefore, τ_S is a computation of the local scattering time only and does not represent the time required to accumulate the overall distribution of He^+. The ratio $\tau_G/\tau_S \simeq 1$ with significant variation. We postulate that the observation of $E_{\rm lip} > 0$ and $|E_{\rm lip}| < 0.35$ might be the result of incomplete PUI scattering, but this plot does not support that interpretation.

3.3. Turbulent Cascade

Most now agree that interplanetary solar wind and magnetic field fluctuations evolve as a turbulent MHD flow. Agreement can be shown between the measured spectrum of fluctuations and the inferred rate of thermal proton heating using simple turbulent scaling laws (Vasquez et al. 2007; Lamarche et al. 2014; Montagud-Camps et al. 2018). Turbulent transport theory successfully reproduced the fluctuation power, correlation length, cross helicity, and proton heating from 0.3 to 100 au at both high and low latitudes (Zhou & Matthaeus 1990a, 1990b; Matthaeus et al. 1994; Zank et al. 1996, 2012, 2017; Smith et al. 2001, 2006b; Isenberg et al. 2003, 2010; Breech et al. 2005, 2008, 2009, 2010; Isenberg 2005; Usmanov & Goldstein 2006; Ng et al. 2010; Usmanov et al. 2011, 2012, 2014a, 2014b, 2018; Oughton et al. 2011; Adhikari et al. 2015a, 2015b, 2017).

The dynamics of the turbulent cascade, though the subject of significant debate, act to remake the fluctuation energy on decreasing temporal and spatial scales. This moves the energy from the largest scales, those associated with transient flow, to the smallest scales, those associated with kinetic dissipation. Ultimately, turbulent fluctuations provide the energy that heats the background plasma. Third-moment theory has provided a very general technique for measuring the rate of energy cascade through the turbulent inertial range (Kolmogorov 1941b; Politano & Pouquet 1998a, 1998b). It has been shown to agree with the rate of thermal proton heating (MacBride et al. 2008; Stawarz et al. 2009; Coburn et al. 2012; Hadid et al. 2017).

Each theory for turbulent dynamics varies in both the timescales for the transport of energy through the spectrum and the characteristic lifetimes of the individual fluctuations. We are adopting the most traditional view. This view has come to be recognized as a likely explanation for the dominant two-dimensional fluctuations with wavevectors that are quasi-perpendicular to the mean magnetic field (Bieber et al. 1996; Leamon et al. 1998a, 1998b; Dasso et al. 2005; Hamilton et al. 2008; MacBride et al. 2010). An extension of the hydrodynamic theory of Kolmogorov (1941a) adapted for MHD (Matthaeus & Zhou 1989; Leamon et al. 1999; Smith 2009; Matthaeus & Velli 2011) predicts the rate of energy transport through the spatial scales that constitute the inertial range by using the amplitude of the power spectrum. The overall amplitude of the cascade rate is rescaled to match the observed proton heating rate in order to obtain (Vasquez et al. 2007; Montagud-Camps et al. 2018):

$$\epsilon = \frac{f^{5/2}\,[E(f)]^{3/2} \cdot 21.8^3}{V_{\rm SW} N_P^{3/2}}, \tag{4}$$

where $E(f)$ is the measured magnetic field power spectral density in units of $\mathrm{nT^2\,Hz^{-1}}$. It is assumed to vary as $f^{-5/3}$. N_P and 21.8^3 are part of the conversion of the magnetic field to Alfvén units, and ϵ is given in units of $\mathrm{km^2\,s^{-3}}$. We assume equipartition of kinetic and magnetic energy so that the Alfvén ratio is $R_{\rm A} = 1$.

Not only do the power spectra studied here vary significantly in intensity, they also do not show background power laws that agree with the $f^{-5/3}$ prediction assumed consistently above. This power-law index variation could result from the use of relatively short data intervals. Data intervals are often short, because wave events in the data often have a brief duration. Averages of large volumes of data do not regularly agree with short samples of said data. We also understand that measurement noise leads to flattened spectra when the overall spectral amplitude is sufficiently reduced as can be seen in the Voyager data (Behannon et al. 1977; Argall et al. 2017) and demonstrated here in the Appendix. We believe that the above scaling of the cascade remains a reasonable starting point for the application of turbulence ideas.

Figure 11 shows our analysis of the turbulence and wave growth rates. The top panel shows the computed turbulence rates using Equation (4). This is the computed average rate at which energy moves through the inertial range of the turbulence. As such, it provides a rate for remaking any energy that is injected into scales of the inertial range. The slower the turbulence rate, the more time the turbulence allows for the accumulation of wave energy. The rates are strongly dependent upon the heliocentric distance, which is consistent with waves (red triangles) appearing most often in more distant measurements in Figure 8. As stated before, they are noticeably absent from the fast-latitude scans during the solar minimum (1994–95 and 2007–09) when the turbulence rate is highest, but are relatively more common during the fast scans of the solar maximum (2001). This appears to be because the range of time when the turbulence is elevated is smaller, and the enhanced turbulence rates are restricted to a more narrow band about 0° latitude. The broad structure of the turbulence rates associated with the fast scans of the solar minimum are distinctly different from the narrow peak in the solar maximum scan. These differences are interesting because they point beyond the physics of pickup ion scattering and wave excitation, directly to the latitudinal extent of the low-latitude turbulence as it varies with the solar cycle.

Figure 11 (middle) shows the wave energy growth rates in the H^+ frequency range for the same intervals. The rates are computed using the formalism in Sections 3.1 and 3.2. The wave growth rate for the control intervals varies weakly with the solar cycle and heliocentric distance. Neutral He ionization is primarily the result of collision with solar EUV photons. It appears that neutral He density is sufficiently dependent upon the heliocentric distance to compensate approximately for the R^{-2} dependence of solar EUV radiation. At the same time, it is evident that the wave growth rate for the wave events is generally elevated relative to the background intervals.

Figure 11 (bottom) shows the ratio of the wave growth to turbulence rates. This panel clearly shows that waves are seen when the growth rate is comparable to or exceeds the turbulence rate. Comparison of the panels shows that the ability to observe the waves depends more on the changing turbulence rates than on any changing wave growth rates. The interpretation of these results is that waves are continuously excited by newborn interstellar PUIs but can only be observed when the growth rate overcomes the background turbulence.

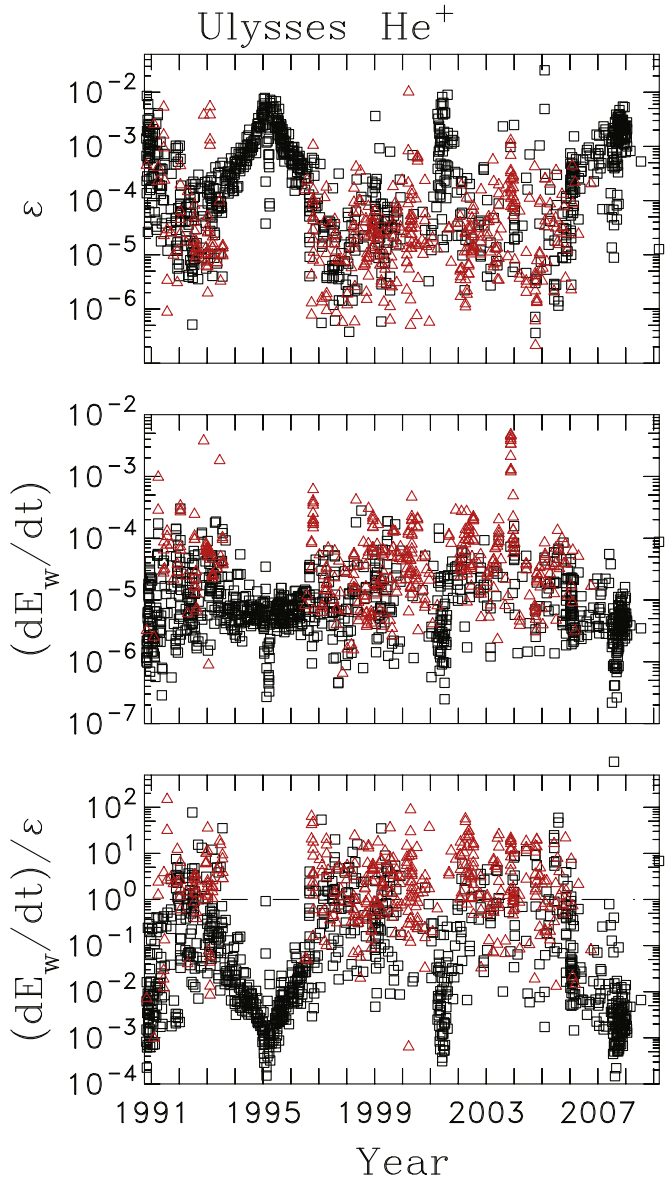

Figure 11. (top) Turbulent energy transport rate ϵ in units of km^2 s^{-3} evaluated using the background spectrum (minus any enhanced wave power due to suprathermal ions) evaluated at $f_{He,c}$. (middle) Wave excitation rate (dE_W/dt) for newborn interstellar pickup He$^+$ in units of km^2 s^{-3}. (bottom) Ratio of rates showing that wave growth is favored outside the fast latitude scans. This means when the spacecraft is at lower latitudes and greater heliocentric distances.

Figure 12 plots the ratio of the wave growth to turbulence rates as a function of the ellipticity of the waves. This demonstrates that the control intervals are generally of low ellipticity ($E_{lip} \simeq 0$). Waves tend to be left-hand polarized in the spacecraft frame, although there are exceptions. They are seen when the growth rate is comparable to or greater than the turbulence rate, although a more representative threshold might be $dE_W/dt/\epsilon > 0.1$. This lower threshold was observed by Voyager for waves due to pickup He$^+$ beyond 10 au. Some wave events are right-hand polarized, and most notably, some have $E_{lip} \simeq 0$.

4. Summary

When interstellar neutral atoms become ionized in the heliosphere, they begin interacting with the heliospheric

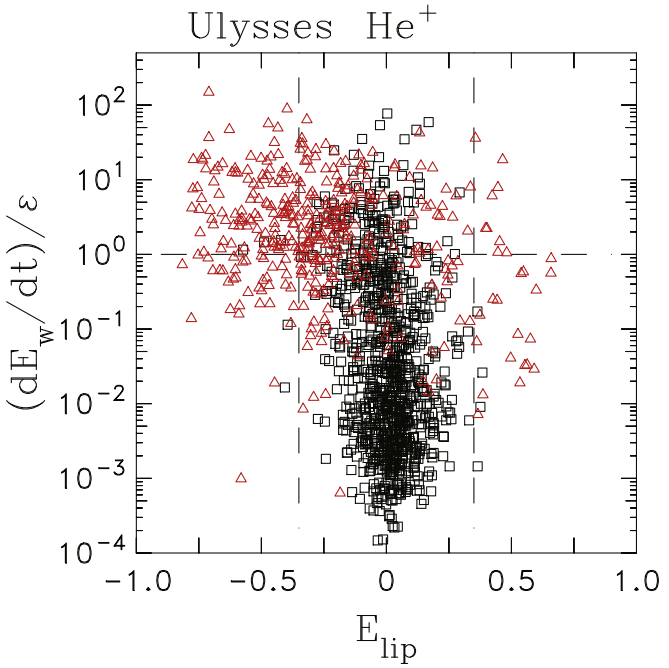

Figure 12. The ratio of the wave growth rate to the turbulence rate ($dE_W/dt)/\epsilon$ showing that waves, as represented by times of high $E_{lip} < -0.25$, are seen during times of favorable growth rates. However, the figure also demonstrates that times of favorable growth rate can exhibit little or complex polarization signatures that suggest processes outside the normal description of wave excitation.

plasma. These newborn pickup ions stream along the local magnetic field and excite low-frequency magnetic waves as they scatter to greater pitch angles. We have reported observations of these waves by the Ulysses spacecraft that arise from newborn interstellar pickup He$^+$. They are observed when the background turbulence is weaker than the wave growth, thereby allowing the wave energy to accumulate over the relatively long times that the low growth rates require. To find wave events, we used one-second magnetic field observations to create daily spectrograms. The most reliable way to analyze these spectrograms for wave events is to look for large bands of uniform color in the ellipticity panel, rather than inspect the power spectrum. The data intervals are then chosen from the selected times of wave events seen in the spectrograms and reanalyzed using a library of preexisting spectral codes. In the figures here, we distinguish the control intervals as black squares and the wave events as red triangles. In some figures, green circles are those events that show strong wave activity, and blue plusses are those that are suggestive of an energized H$^+$ source.

As has been shown in past studies, background turbulence can overwhelm the accumulation of wave energy, transporting it to smaller scales, and eventually heating the background plasma. When the turbulence is weak and the rate is low, wave energy can accumulate over time until it becomes observable. The wave growth time is generally long when compared to the timescale of scattering individual ions (Cannon et al. 2014b), so we postulate that the accumulation of pickup ions and their associated wave energy pass through quasi-stationary asymptotic states, as predicted by Lee & Ip (1987). We compute the derivative of this theoretical quantity numerically using PUI production rates based on established interstellar neutral species densities and known ionization dynamics. When

calculating the production rates, we also use measurements of solar wind parameters from the Ulysses SWOOPS instrument. To find the wave growth rates, we apply the wave excitation theory of Lee & Ip (1987) to the computed PUI production rates. Then, by assuming the rate is slow compared to the scattering, we use those formulas to evaluate the growth of wave energy as PUI density increases.

It is noteworthy that wave events are largely absent from the fast-latitude scans during the solar minimum and more common during the fast scans of the solar maximum. The turbulence rate is elevated over a broader range of heliolatitudes during the solar minimum, and during the solar maximum the turbulence is elevated for less time within the data, being restricted to a narrower band of latitudes around 0°. This indicates that the way turbulence varies with the solar cycle and latitude affects the frequency of wave events beyond the physics of PUI scattering and wave excitation.

P.A.I., B.J.V., and C.W.S. are supported by NASA grants 80NSSC18K1215 and 80NSSC17K0009. P.A.I. and B.J.V. are also supported by NSF grant AGS2005982. B.J.V. is supported by NSF grant AGS1357893. C.J.J. was partially supported by NASA SR&T grant NNG06GD55G and the Sun-2-Ice (NSF grant No. AGS1135432) project. M.B. and M.A.K. acknowledge support by the Polish National Science Center grant 2019-35-B-ST9-01241. The data used in this analysis are available from the NSSDC.

Appendix
Time Interval Listings

The wave event lists for strong and weak wave observations due to pickup He^+ are given in Tables 1 and 2, respectively. We omit listing the control intervals since these can be found throughout the Ulysses catalog. We also omit listing the times when we suspect there is energization of the pickup H^+ ions as the detailed analysis of these intervals lies outside the realm of this paper.

Table 1
Ulysses Observations of Waves due to Pickup He^+: $|E_{lip}| > 0.35$

Year	Time [DOY::Hour:Min]	E_{lip}	Time [DOY::Hour:Min]	E_{lip}	Time [DOY::Hour:Min]	E_{lip}
1990	302/09:01–16:01	0.37				
1991	036/00:00–03:00	−0.58	089/02:00–07:00	−0.36	090/02:00–04:01	−0.59
	161/04:01–09:01	0.59	161/00:00–12:00	0.53	206/08:01–14:01	−0.71
	206/00:00–23:02	−0.45	256/11:00–16:01	−0.58	289/00:00–10:00	0.40
	339/19:02–23:02	−0.59				
1992	014/10:01–12:01	−0.67	015/00:00–04:01	−0.69	015/06:02–14:01	−0.49
	089/13:00–18:00	−0.41	109/05:01–13:00	0.50	197/00:00–04:01	0.66
	200/00:00–04:01	−0.70	200/12:00–18:00	−0.60	200/00:00–23:01	−0.58
	201/00:00–07:01	−0.74	217/00:00–05:01	−0.38	221/03:00–06:00	−0.43
	225/09:00–14:01	−0.40	225/18:00–22:01	−0.40	351/16:01–21:01	0.42
	353/13:02–16:00	−0.49	353/17:00–23:02	−0.55	353/14:01–23:02	−0.53
1993	006/00:00–04:01	−0.47	006/00:00–21:01	−0.43	006/00:00–12:00	−0.45
	070/02:02–13:00	−0.37	071/02:00–06:01	0.45	071/07:01–11:00	0.48
	163/10:02–12:01	0.47	204/07:00–19:00	−0.59	204/09:02–16:01	−0.64
	204/09:01–19:00	−0.70				
1996	291/20:00–23:01	−0.59	270/16:01–23:02	−0.54	291/00:00–03:00	−0.53
	291/06:00–12:02	−0.42	291/15:00–18:01	−0.63	291/00:00–23:02	−0.58
	292/12:00–17:01	−0.52	292/00:00–23:02	−0.41	293/00:00–04:01	−0.45
1997	043/06:00–07:00	−0.75	043/06:00–08:02	−0.41	076/03:00–04:00	−0.65
	103/13:00–15:01	−0.43	194/06:00–09:00	−0.49	208/17:01–21:02	−0.62
	231/00:00–02:02	−0.48	263/21:01–23:02	−0.36		
1998	007/04:00–06:00	−0.54	007/00:00–14:01	−0.40	062/00:01–04:00	−0.50
	091/08:00–09:01	−0.63	091/11:01–12:01	−0.75	091/18:00–21:01	−0.66
	091/07:00–21:01	−0.67	095/12:01–14:01	0.60	095/02:00–19:00	0.66
	153/18:00–20:01	−0.55	163/03:02–06:00	−0.51	219/09:01–10:02	−0.60
	240/21:01–23:02	−0.48	251/10:02–14:01	−0.71	251/14:02–19:02	−0.38
	256/15:02–16:01	−0.55	266/09:00–12:00	−0.47	284/07:01–09:01	−0.59
	285/00:00–06:02	−0.67	285/21:01–23:02	−0.69	322/05:01–06:01	−0.78
	322/07:02–12:01	−0.59	322/00:00–14:01	−0.51	342/01:00–03:01	−0.69
	342/04:01–09:01	−0.48	342/20:01–23:02	−0.46	342/21:01–22:01	−0.38
	343/00:00–05:00	−0.51	343/01:01–04:00	−0.39	343/00:00–14:01	−0.41
1999	045/00:00–03:02	−0.48	102/00:00–03:02	−0.56	102/00:00–09:01	−0.48
	128/04:01–07:01	−0.60	202/11:01–14:01	−0.40	203/00:00–06:02	0.36
	226/07:00–20:01	−0.48	240/15:01–19:01	−0.82	244/00:00–05:01	−0.76
	244/06:02–12:01	−0.66	325/06:00–09:00	−0.35	338/14:00–17:01	0.40
	359/18:00–21:00	−0.62				
2000	075/10:00–14:02	0.54	075/16:01–21:00	0.37	105/21:02–23:01	−0.40
	106/16:00–18:01	−0.38	121/10:02–14:00	−0.38	121/14:02–23:02	−0.41
	122/13:02–17:00	−0.43	123/02:01–10:02	−0.37	123/04:00–10:01	−0.41
	257/02:00–03:02	−0.45	293/19:01–23:02	0.44	294/00:00–00:00	0.55
	296/22:01–23:02	−0.37	317/00:00–02:00	−0.52	351/20:00–23:02	−0.39
	352/07:02–12:01	−0.71				
2001	242/07:00–21:02	−0.42	242/12:00–22:01	−0.40	331/22:00–23:00	−0.77
2002	023/13:02–16:01	−0.35	024/20:01–23:00	−0.69	029/05:00–16:00	−0.45
	041/13:01–19:01	−0.46	047/11:00–14:02	−0.40	080/00:00–06:00	−0.36
	093/07:00–12:00	−0.43	093/07:00–14:01	−0.47	108/01:00–04:00	−0.61
	171/15:02–23:02	−0.51	171/01:01–05:01	−0.38	171/16:01–23:02	−0.54
	292/00:01–02:00	−0.40	297/19:00–21:01	0.55	298/11:02–13:01	0.56
2003	012/19:00–23:02	0.45	087/18:02–21:00	0.58	164/00:00–08:00	−0.57
	165/00:00–08:01	−0.45	165/09:01–20:01	−0.47	193/13:02–18:01	−0.65
	247/00:00–11:00	0.36	320/03:01–08:00	−0.51	320/09:00–19:01	−0.78
	320/20:01–23:02	−0.74	321/00:00–09:00	−0.60	321/00:00–08:01	−0.62
	321/09:01–16:01	−0.72	321/10:01–16:01	−0.74	321/17:00–23:01	−0.73
	321/17:01–23:02	−0.77	322/00:00–09:00	−0.51	322/06:00–09:00	−0.66
	322/19:01–23:01	−0.50	351/14:01–17:01	−0.61	351/19:00–23:02	−0.56
	351/19:00–23:02	−0.57	352/00:00–03:01	−0.73	352/00:00–07:00	−0.50
	352/07:01–17:01	−0.61	352/12:00–13:02	−0.44	352/18:02–23:02	−0.32
	353/00:00–06:02	−0.45				
2004	008/07:00–14:01	−0.60	071/10:01–16:01	−0.41	072/00:00–08:00	−0.49
	073/21:01–23:01	0.53	159/10:01–19:01	−0.41	159/12:00–19:00	−0.55
	269/00:02–04:01	−0.45	278/04:01–14:01	−0.45	297/11:00–16:01	−0.72
	297/17:01–23:02	−0.50	297/17:02–23:02	−0.46	335/13:01–16:01	0.43
2005	041/00:00–04:01	−0.37	041/01:00–04:01	−0.47	061/19:00–23:02	−0.37
	104/10:02–19:00	−0.42	185/00:00–02:00	0.39	203/05:00–09:01	0.45
	307/00:00–04:01	−0.43				

Table 2
Ulysses Observations of Waves due to Pickup He^+: $|E_{lip}| < 0.35$

Year	Time [DOY::Hour:Min]	E_{lip}	Time [DOY::Hour:Min]	E_{lip}	Time [DOY::Hour:Min]	E_{lip}
1991	161/17:01–19:01	−0.29	164/10:01–15:02	−0.31	172/10:00–14:01	−0.06
	206/16:01–22:01	−0.24	340/01:01–07:00	−0.20		
1992	014/16:01–23:02	−0.27	015/15:00–22:01	−0.25	219/19:00–23:01	−0.31
	220/02:00–07:00	−0.07				
1992	220/20:02–23:02	0.07	320/10:02–19:00	−0.05	346/16:00–23:02	0.04
1993	005/01:00–06:00	0.20	005/10:02–21:01	−0.17	006/12:00–21:01	−0.34
	007/01:00–07:02	0.01	018/00:00–07:00	0.00	037/00:00–04:01	−0.32
	037/07:00–13:01	−0.33	037/00:00–16:01	−0.12	037/04:01–14:01	−0.24
	070/04:01–16:01	−0.26	070/03:01–18:00	−0.26	129/12:01–15:01	0.22
	129/12:00–19:00	0.18	175/15:00–18:01	−0.10	200/14:01–23:02	−0.24
	200/14:01–22:01	−0.19				
1996	186/00:00–06:01	0.01	213/03:00–05:00	0.18	271/07:00–12:00	0.13
	271/14:01–15:01	−0.32	290/15:01–22:00	−0.21	290/14:01–23:02	−0.18
	292/00:00–07:02	−0.16	296/12:00–14:01	−0.21		
1997	008/00:00–16:01	−0.34	045/04:01–14:01	−0.31	076/00:00–09:01	−0.29
	099/00:00–03:01	−0.30	099/07:01–10:02	−0.28	099/00:00–19:00	−0.27
	101/19:02–20:02	0.14	123/03:01–05:01	0.16	147/09:01–15:00	−0.31
	207/07:00–10:02	−0.32	230/17:01–19:02	−0.34	230/14:01–23:02	−0.23
	235/04:01–16:01	−0.29	281/00:00–12:00	−0.27	311/09:01–19:00	0.17
	341/00:00–12:00	−0.20				
1998	001/03:01–09:01	−0.20	088/09:01–19:00	−0.26	095/02:00–04:01	0.21
	104/09:00–11:00	−0.21	106/00:02–05:00	−0.29	122/13:01–15:01	−0.20
	153/14:01–21:01	0.06	178/04:01–12:00	0.23	178/00:00–12:00	0.15
	238/12:02–15:01	−0.16	238/09:01–23:02	−0.14	261/09:00–12:00	−0.27
	261/19:00–23:02	−0.23	266/00:00–12:00	−0.08	272/15:01–18:00	0.28
	321/12:00–19:00	−0.34	322/13:00–15:01	−0.26	341/20:01–23:02	−0.32
	358/02:00–12:00	−0.27				
1999	007/13:00–16:01	−0.32	012/02:00–07:00	0.24	032/12:00–18:01	−0.31
	042/20:01–23:00	−0.27	042/14:01–23:02	−0.13	070/02:00–06:02	0.13
	087/15:00–23:02	−0.10	087/12:00–23:02	−0.16	098/21:01–23:02	−0.15
	101/20:01–23:02	−0.30	107/07:00–18:00	−0.31	113/07:00–16:01	0.33
	121/12:00–23:02	−0.06	136/13:00–23:02	−0.13	203/02:00–06:01	0.34
	221/08:00–12:01	−0.30	229/07:00–13:02	−0.28	229/10:02–13:00	−0.24
	243/20:01–23:02	−0.22	243/21:00–23:02	−0.24	269/10:00–12:02	−0.34
	270/21:00–23:02	−0.23	289/04:01–16:01	−0.16	299/12:00–15:01	−0.13
	299/16:01–21:00	−0.07	351/02:01–09:02	0.12		
2000	046/19:01–23:02	−0.21	056/15:00–23:02	0.03	056/19:01–23:02	−0.06
	057/00:00–02:00	−0.13	057/00:00–05:01	−0.19	057/07:00–16:01	−0.15
	073/10:02–15:01	−0.26	080/19:01–21:00	−0.19	085/17:00–23:00	−0.18
	105/21:01–23:02	−0.24	106/00:00–03:00	−0.19	106/00:00–07:01	−0.35
	106/05:00–07:01	−0.22	106/09:01–14:01	0.18	106/09:01–14:01	0.18
	106/16:00–21:01	−0.28	121/10:02–14:00	−0.38	122/00:01–03:00	−0.34
	122/01:01–03:00	−0.17	122/06:00–12:01	−0.17	122/14:00–23:02	−0.26
	123/12:00–16:00	−0.28	174/12:00–23:02	0.11	175/00:00–09:02	−0.19
	175/11:01–14:01	0.22	175/10:02–16:01	0.05	187/18:00–21:00	−0.10
	197/02:00–09:01	0.00	197/04:01–09:00	0.05	197/09:02–18:01	−0.23
	197/13:00–18:00	−0.25	204/02:00–07:02	−0.33	209/02:00–04:01	−0.23
	269/04:01–08:00	−0.31	297/09:00–11:00	−0.06		
2001	029/06:00–07:01	−0.33	091/02:01–04:01	0.24	271/21:00–22:00	−0.20
2002	023/08:01–12:00	−0.29	028/07:00–17:00	−0.19	028/09:02–19:02	−0.33
	029/02:00–04:01	−0.24	092/11:00–15:00	−0.20	093/15:02–23:01	−0.05
	094/00:00–02:00	−0.07	113/16:00–23:02	−0.21	113/18:01–23:02	−0.30
	114/01:00–07:01	0.29	136/14:01–17:01	−0.05	136/18:02–23:01	−0.34
	136/19:00–23:02	−0.34	137/00:00–03:02	−0.31	137/14:00–20:01	−0.16
	137/16:01–21:01	−0.34	172/00:00–02:02	−0.14	179/16:01–20:00	−0.10
	195/07:00–16:01	−0.24	196/06:01–11:00	−0.30	196/06:01–11:01	−0.30
	196/12:00–23:02	−0.18	196/12:00–23:01	−0.24	197/00:00–02:00	−0.34
	197/00:00–13:01	0.03	197/03:00–06:00	0.20	197/14:00–20:01	−0.21
	266/10:00–11:00	0.03	292/07:01–10:00	−0.21		
2003	012/11:00–23:02	0.13	012/12:00–18:00	−0.12	032/16:01–23:02	−0.34

Table 2
(Continued)

Year	Time [DOY::Hour:Min]	E_{lip}	Time [DOY::Hour:Min]	E_{lip}	Time [DOY::Hour:Min]	E_{lip}
	035/14:01–19:01	0.29	056/15:01–19:00	−0.34	097/06:01–18:02	−0.18
	097/06:02–19:00	−0.12	098/04:02–07:00	0.25	098/08:00–12:01	−0.17
	117/00:00–04:01	0.14	117/09:00–13:01	0.25	120/01:00–07:00	−0.21
	132/16:01–22:01	−0.17	146/09:00–23:00	−0.01	147/00:00–09:01	−0.11
	147/18:00–22:01	−0.24	164/09:01–22:01	−0.13	165/19:01–22:01	−0.35
	251/21:00–23:01	0.33	282/14:01–19:00	−0.35	352/18:02–23:02	−0.32
	353/07:01–16:01	−0.28				
2004	008/00:00–06:00	−0.08	159/02:00–09:01	−0.32	159/07:00–10:02	0.01
	202/12:01–18:00	0.01	277/21:00–23:02	0.09	279/00:00–10:02	−0.08
	279/15:00–22:00	0.19	283/00:00–02:00	−0.22	283/00:00–03:00	−0.06
	298/00:00–02:00	−0.30	335/09:00–12:00	0.27	335/09:00–12:00	0.11
	343/19:00–23:02	−0.13	344/00:00–02:00	−0.14		
2005	004/08:00–16:01	−0.17	010/21:00–23:02	0.26	033/07:00–12:00	−0.30
	040/13:02–23:02	−0.29	104/10:01–23:00	−0.25	106/00:00–07:01	−0.12
	158/18:02–21:02	−0.09	160/00:00–05:02	0.05	179/00:00–08:02	−0.20
	179/09:01–17:01	−0.24	224/16:01–21:01	−0.23	227/09:01–14:01	−0.34
	261/10:01–14:01	−0.28	264/06:00–13:00	−0.31	289/00:01–15:01	−0.22
	315/17:00–23:02	−0.16	333/16:01–23:02	−0.08		
2006	017/12:02–17:00	0.24	033/00:00–08:01	0.20	037/19:00–23:02	0.11
	069/02:00–05:00	0.17	112/19:01–21:02	0.07	275/09:02–12:00	−0.30

ORCID iDs

Anastasia V. Marchuk https://orcid.org/0000-0002-7408-5671
Charles W. Smith https://orcid.org/0000-0002-5379-1542
Abigale S. Watson https://orcid.org/0000-0003-2057-5891
Matthew R. Argall https://orcid.org/0000-0001-6315-1613
Colin J. Joyce https://orcid.org/0000-0002-3841-5020
Philip A. Isenberg https://orcid.org/0000-0003-0505-8546
Bernard J. Vasquez https://orcid.org/0000-0001-8593-7289
Nathan A. Schwadron https://orcid.org/0000-0002-3737-9283
Maciej Bzowski https://orcid.org/0000-0003-3957-2359
Marzena A. Kubiak https://orcid.org/0000-0002-5204-9645

References

Adhikari, L., Zank, G. P., Bruno, R., et al. 2015a, ApJ, 805, 63
Adhikari, L., Zank, G. P., Bruno, R., et al. 2015b, JPhCS, 642, 012001
Adhikari, L., Zank, G. P., Hunana, P., et al. 2017, ApJ, 841, 85
Aggarwal, P., Taylor, D. K., Smith, C. W., et al. 2016, ApJ, 822, 94
Argall, M. R., Fisher, M. F., Joyce, C. J., et al. 2015, GeoRL, 42, 9617
Argall, M. R., Hollick, S. J., Pine, Z. B., et al. 2017, ApJ, 849, 61
Argall, M. R., Hollick, S. J., Pine, Z. B., et al. 2018, ApJ, 854, 77
Behannon, K. W., Acuña, M. H., Burlaga, L. F., et al. 1977, SSRv, 21, 235
Bieber, J. W., Wanner, W., & Matthaeus, W. H. 1996, JGR, 101, 2511
Blackman, R. B., & Tukey, J. W. 1958, The Measurement of Power Spectra (Mineola, NY: Dover)
Breech, B., Cranmer, S. R., Matthaeus, W. H., Kasper, J. C., & Oughton, S. 2010, in AIP Conf. Proc. 1216, Twelfth Int. Solar Wind Conf., ed. M. Maksimovic et al. (Melville, NY: AIP), 214
Breech, B., Matthaeus, W. H., Cranmer, S. R., Kasper, J. C., & Oughton, S. 2009, JGRA, 114, A09103
Breech, B., Matthaeus, W. H., Minnie, J., et al. 2005, GeoRL, 32, L06103
Breech, B., Matthaeus, W. H., Minnie, J., et al. 2008, JGRA, 113, A08105
Bzowski, M., Kubiak, M. A., Möbius, E., et al. 2012, ApJS, 198, 12
Bzowski, M., Swaczyna, P., Kubiak, M. A., et al. 2015, ApJS, 220, 28
Cannon, B. E., Smith, C. W., Isenberg, P. A., et al. 2013, in AIP Conf. Proc. 1539, Solar Wind 13, ed. G. P. Zank et al. (Melville, NY: AIP), 334
Cannon, B. E., Smith, C. W., Isenberg, P. A., et al. 2014a, ApJ, 784, 150
Cannon, B. E., Smith, C. W., Isenberg, P. A., et al. 2014b, ApJ, 787, 133
Cannon, B. E., Smith, C. W., Isenberg, P. A., et al. 2017, ApJ, 840, 13
Chen, J. 1989, PhD thesis, Univ. of Delaware
Coburn, J. T., Smith, C. W., Vasquez, B. J., Stawarz, J. E., & Forman, M. A. 2012, ApJ, 754, 93
Dasso, S., Milano, L. J., Matthaeus, W. H., & Smith, C. W. 2005, ApJL, 635, L181
Fahr, H. J. 1978, A&A, 66, 103
Fahr, H. J. 1979, A&A, 77, 101
Fisher, M. K., Argall, M. R., Joyce, C. J., et al. 2016, ApJ, 830, 47
Fowler, R. A., Kotick, B. J., & Elliott, R. D. 1967, JGR, 72, 2871
Hadid, L. Z., Sahraoui, F., & Galtier, S. 2017, ApJ, 838, 9
Hamilton, K., Smith, C. W., Vasquez, B. J., & Leamon, R. J. 2008, JGRA, 113, A01106
Hollick, S. J., Smith, C. W., Pine, Z. B., et al. 2018a, ApJ, 863, 75
Hollick, S. J., Smith, C. W., Pine, Z. B., et al. 2018b, ApJ, 863, 76
Hollick, S. J., Smith, C. W., Pine, Z. B., et al. 2018c, ApJS, 237, 34
Isenberg, P. A. 2005, ApJ, 623, 502
Isenberg, P. A., Smith, C. W., & Matthaeus, W. H. 2003, ApJ, 592, 564
Isenberg, P. A., Smith, C. W., Matthaeus, W. H., & Richardson, J. D. 2010, ApJ, 719, 716
Joyce, C. J., Smith, C. W., Isenberg, P. A., et al. 2012, ApJ, 745, 112
Joyce, C. J., Smith, C. W., Isenberg, P. A., Murphy, N., & Schwadron, N. A. 2010, ApJ, 724, 1256
King, J. H., & Papitashvili, N. E. 2005, JGRA, 110, A02104
Kolmogorov, A. N. 1941a, DoSSR, 30, 301
Kolmogorov, A. N. 1941b, DoSSR, 32, 16
Kowalska-Leszczynska, I., Bzowski, M., Kubiak, M. A., & Sokół, J. M. 2020, ApJS, 247, 62
Lamarche, L. J., Vasquez, B. J., & Smith, C. W. 2014, JGRA, 119, 3267
Leamon, R. J., Smith, C. W., & Ness, N. F. 1998a, GeoRL, 25, 2505
Leamon, R. J., Smith, C. W., Ness, N. F., Matthaeus, W. H., & Wong, H. K. 1998b, JGR, 103, 4775
Leamon, R. J., Smith, C. W., Ness, N. F., & Wong, H. K. 1999, JGR, 104, 22331
Lee, M. A., & Ip, W.-H. 1987, JGR, 92, 11041
MacBride, B. T., Smith, C. W., & Forman, M. A. 2008, ApJ, 679, 1644
MacBride, B. T., Smith, C. W., & Vasquez, B. J. 2010, JGRA, 115, A07105
Markovskii, S. A., Vasquez, B. J., & Smith, C. W. 2008, ApJ, 675, 1576
Markovskii, S. A., Vasquez, B. J., & Smith, C. W. 2015, ApJ, 806, 78
Matthaeus, W. H., & Goldstein, M. L. 1982, JGR, 87, 6011
Matthaeus, W. H., Oughton, S., Pontius, D. H., Jr., & Zhou, Y. 1994, JGR, 99, 19267
Matthaeus, W. H., & Velli, M. 2011, SSRv, 160, 145
Matthaeus, W. H., & Zhou, Y. 1989, PhFlB, 1, 1929
McComas, D. J., Alexashov, D., Bzowski, H., et al. 2012, Sci, 336, 1291
McComas, D. J., Bzowski, M., Fuselier, S. A., et al. 2015, ApJS, 220, 22
McComas, D. J., Zirnstein, E. J., Bzowski, M., et al. 2017, ApJS, 233, 8

Means, J. D. 1972, JGR, 77, 5551
Mish, W. H., Wenger, R. M., Behannon, K. W., & Byrnes, J. B. 1982, Interactive Digital Signal Processor, NASA Technical Memorandum 83997 (Greenbelt, MD: Goddard Space Flight Center)
Möbius, E., Bochsler, P., Bzowski, M., et al. 2012, ApJS, 198, 11
Montagud-Camps, V., Grappin, R., & Verdini, A. 2018, ApJ, 853, 153
Murphy, N., Smith, E. J., Tsurutani, B. T., Balogh, A., & Southwood, D. J. 1995, SSRv, 72, 447
Ng, C. S., Bhattacharjee, A., Munsi, D., Isenberg, P. A., & Smith, C. W. 2010, JGRA, 115, A02101
Oughton, S., Matthaeus, W. H., Smith, C. W., Breech, B., & Isenberg, P. A. 2011, JGRA, 116, A08105
Pine, Z. B., Smith, C. W., Hollick, S. J., et al. 2020, ApJ, 900, 94
Politano, H., & Pouquet, A. 1998a, PhRvE, 57, R21
Politano, H., & Pouquet, A. 1998b, GeoRL, 25, 273
Rankin, D., & Kurtz, R. 1970, JGR, 75, 5444
Schwadron, N. A., Möbius, E., Leonard, T., et al. 2015, ApJS, 220, 25
Smith, C. W. 2009, in Heliophysics I. Plasma Physics of the Local Cosmos, ed. C. J. Schrijver & G. Siscoe (Cambridge: Cambridge Univ. Press)
Smith, C. W., Aggarwal, P., Argall, M. R., et al. 2017, JPhCS, 900, 012018
Smith, C. W., Hamilton, K., Vasquez, B. J., & Leamon, R. J. 2006a, ApJL, 645, L85
Smith, C. W., Isenberg, P. A., Matthaeus, W. H., & Richardson, J. D. 2006b, ApJ, 638, 508
Smith, C. W., Matthaeus, W. H., & Ness, N. F. 1990, ICRC (Adelaide), 5, 280
Smith, C. W., Matthaeus, W. H., Zank, G. P., et al. 2001, JGR, 106, 8253
Smith, C. W., Vasquez, B. J., & Hamilton, K. 2006c, JGRA, 111, A09111
Sokół, J. M., Kubiak, M. A., Bzowski, M., & Swaczyna, P. 2015, ApJS, 220, 27
Sokół, J. M., McComas, D. J., Bzowski, M., & Tokumaru, M. 2020, ApJ, 897, 179
Stawarz, J. E., Smith, C. W., Vasquez, B. J., Forman, M. A., & MacBride, B. T. 2009, ApJ, 697, 1119
Tarnopolski, S., & Bzowski, M. 2009, A&A, 493, 207
Usmanov, A. V., & Goldstein, M. L. 2006, JGRA, 111, A07101
Usmanov, A. V., Goldstein, M. L., & Matthaeus, W. H. 2012, ApJ, 754, 40
Usmanov, A. V., Goldstein, M. L., & Matthaeus, W. H. 2014a, ApJ, 788, 43
Usmanov, A. V., Goldstein, M. L., & Matthaeus, W. H. 2014b, ApJ, 820, 17
Usmanov, A. V., Matthaeus, W. H., Breech, B. A., & Goldstein, M. L. 2011, ApJ, 727, 84
Usmanov, A. V., Matthaeus, W. H., Goldstein, M. L., & Chhiber, R. 2018, ApJ, 865, 25
Vasquez, B. J., Smith, C. W., Hamilton, K., MacBride, B. T., & Leamon, R. J. 2007, JGRA, 112, A07101
Zank, G. P., Adhikari, L., Hunana, P., et al. 2017, ApJ, 835, 147
Zank, G. P., Dosch, A., Hunana, P., et al. 2012, ApJ, 745, 35
Zank, G. P., Matthaeus, W. H., & Smith, C. W. 1996, JGR, 101, 17093
Zhou, Y., & Matthaeus, W. H. 1990a, JGR, 95, 10291
Zhou, Y., & Matthaeus, W. H. 1990b, JGR, 95, 14881